

Detection possibility of continuous gravitational waves from rotating magnetized neutron stars

Mayusree Das,^{*} Banibrata Mukhopadhyay[†]

Joint Astronomy Programme, Department of Physics, Indian Institute of Science, Bangalore 560012, India

Accepted XXX. Received YYY; in original form ZZZ

ABSTRACT

In the past decades, several neutron stars (NSs), particularly pulsars, with mass $M > 2M_{\odot}$ have been observed. On the other hand, the existence of massive white dwarfs (WDs), even violating Chandrasekhar mass-limit, was inferred from the peak luminosities of type Ia supernovae. Hence, there is a generic question of the origin of massive compact objects. Here we explore the existence of massive, magnetized, rotating NSs with soft and steep equation of states (EoSs) by solving axisymmetric stationary stellar equilibria in general relativity. For our purpose, we consider the Einstein equation solver for stellar structure *XNS* code. Such rotating NSs with magnetic field and rotation axes misaligned, hence with non-zero obliquity angle, can emit continuous gravitational waves (GW), which can be detected by upcoming detectors, e.g., Einstein Telescope, etc. We discuss the decays of magnetic field, angular velocity and obliquity angle with time, due to angular momentum extraction by GW and dipole radiation, which determine the timescales related to the GW emission. Further, in the Alfvén timescale, a differentially rotating, massive proto-NS rapidly settles into an uniformly rotating, less massive NS due to magnetic braking and viscosity. These explorations suggest that detecting massive NSs is challenging and sets a timescale for detection. We calculate the signal-to-noise ratio of GW emission, which confirms that any detector cannot detect them immediately, but detectable by Einstein Telescope, Cosmic Explorer over months of integration time, leading to direct detection of NSs.

Key words: gravitational waves – (stars:) neutron stars – stars: magnetic field – stars: rotation – radiation mechanisms: general

1 INTRODUCTION

Recently gravitational wave (GW) has been detected from several binary mergers by LIGO and VIRGO, when either both the components are black hole (BH) or both are neutron star (NS). Also there is an event GW190814, when one is a BH and other could be either a massive NS or a lighter BH. All these events have enlightened GW astronomy (Abbott et al. 2016a, 2017a,b,c; Abbott et al. 2017e, 2019d). A system radiates GW if it has a non-zero time varying quadrupole moment. The binary systems, detected by LIGO/VIRGO, possess time-varying quadrupole moment while merging. However, isolated objects may also have non-zero time varying quadrupole moment if, e.g., they have mountains and holes around surface, misaligned magnetic and rotation axes (obliquity angle non-zero), hence emit continuous GW (CGW) at a certain frequency (Zimmermann & Szedenits 1979). For different possible mechanisms generating CGW, see the review by Riles (2017). In this paper, we consider triaxial sources with violation of axisymmetry because of non-zero obliquity angle (Bonazzola & Gourgoulhon 1996; Jones & Andersson

2002; Ferrari 2010; Franzon & Schramm 2017; Mukhopadhyay et al. 2017).

Kalita & Mukhopadhyay (2019) argued that strong gravitational radiation can be emitted from rotating magnetized NSs and white dwarfs (WDs) even with a small obliquity angle, which can be detected by upcoming GW detectors. While it is known that compact objects in a binary system radiate more powerful GW than CGW, which however can be detected by at a different frequency range (Kalita & Mukhopadhyay 2019) and hence they can be distinguished.

NSs are born with mass $M \sim 1.4M_{\odot}$, on average (Zhang et al. 2011; Miller 2021), from the evolution of stars with masses $10M_{\odot} \lesssim M \lesssim 20M_{\odot}$. However, NSs as accreting millisecond pulsars have higher masses, $M \sim 1.6M_{\odot}$, on average (Zhang et al. 2011; Mukhopadhyay & Bhattacharya 2022). Recently, higher masses of binary NS systems like millisecond pulsars PSR J1614-2230: $M = 1.97 \pm 0.04M_{\odot}$ (Demorest et al. 2010), PSR J0348+0432: $M = 2.01 \pm 0.04M_{\odot}$ (Antoniadis et al. 2013), and PSR J0740+6620: $M = 2.04^{+0.09}_{-0.10}M_{\odot}$ (Cromartie et al. 2020) have been measured. Very recently, a new GW event reported by Ligo-Virgo collaboration as GW190814 (Abbott et al. 2020) was observed with a $22.2 - 24.3M_{\odot}$ black hole and a $2.50 - 2.67M_{\odot}$ secondary component. As the mass of the secondary component of GW190814

^{*} E-mail: mayusreedas@iisc.ac.in

[†] E-mail: bm@iisc.ac.in

lies in the lower mass region of the mass gap ($2.5M_{\odot} < M < 5M_{\odot}$), it can be a candidate for very massive NS. Such high mass NSs can be inferred to be formed due to high magnetic field and rotation (Pili et al. 2014). Chu et al. (2014), Deb et al. (2021) and Rather et al. (2021) showed that increasing anisotropy and magnetic field strength also can support the existence of massive NSs. It is important to mention that the variance of EoS can generate massive NSs as well (Lattimer 2012), but in order to detect the NSs via GW, we need high ellipticity (hence deformation) and thus we necessarily need to introduce NS with high magnetic field and rotation.

Isolated NSs are very lowly luminous objects due to their tiny size and no source of energy. Thus, we have to rely upon their other activities to detect them directly and one of them is their CGW. Interestingly, there has been no detection of CGW from NSs in LIGO, VIRGO, aLIGO, and aVIRGO so far (Abbott et al. 2019b,c; Piccinni et al. 2020). If any of them is detected in the future, e.g., by Einstein Telescope, Cosmic Explorer, etc., depending on its distance from the Earth, their magnetic field can be predicted from ellipticity (the parameter measuring the degree of deformation of the object) related to their GW amplitude. Hence, the detection of CGWs from isolated NSs would be a fundamental breakthrough, which can provide us an idea about their spin, magnetic field, as well as EoS.

One of the potential origins of high magnetic fields in a NS, e.g., magnetar, is the frozen-flux, particularly if the field is not disrupted during the core-collapse of a massive star (Woltjer 1964; Ferrario et al. 2015). However, a strong fossil field brakes stellar rotation (Shultz et al. 2017), hence a fossil field is probably not compatible with the existing fast rotation of NSs. An additional mechanism, like a dynamo (Frisch et al. 1975; Moffatt 1978; Thompson & Duncan 1993; Brandenburg 2001; Bonanno et al. 2003; Brandenburg & Subramanian 2005) or the magnetorotational instability (Fricke 1969; Balbus & Hawley 1991; Obergaulinger et al. 2009; Guilet & Müller 2015; Mösta et al. 2015; Rembiasz et al. 2016), is needed to enhance this fossil field above 10^{15} G. The core of the proto-NS experiences neutrino-driven turbulent convection during the first few tens of seconds (Miralles et al. 2000; Thompson & Murray 2001; Miralles et al. 2002). A strong differential rotation is also present if the proto-NS is generated from merger or remnant of supernovae. Differential rotation along with convection can generate $\alpha - \Omega$ dynamo acting over the whole NS core (Duncan & Thompson 1992). By differential rotation, the frozen poloidal magnetic field is twisted into toroidal field. However, the total kinetic energy available from the core differential rotation corresponds to a maximum field of $\simeq 10^{17-18}$ G, depending on the initial spin period (Thompson & Duncan 1993; Duncan 1998). In slowly rotating NSs, differential rotation is however negligible and a convection-driven α -type dynamo results in a much weaker large-scale field (Duncan & Thompson 1992; Thompson & Duncan 1993).

The rotational frequency and obliquity angle of rotating magnetized NSs decay with time due to the extraction of angular momentum by GW and dipole radiation. Radio astronomers estimate the characteristic lifetime of a pulsar by calculating its observed time period and the rate of change of time period (Lorimer 2008). However, generally this calculation assumes that the obliquity angle remains constant throughout its lifetime, which actually changes due to radia-

tion. However, the spin-down timescale or age was calculated for spherically symmetric stars considering the decays of spin and the obliquity angle simultaneously of the pulsar having dipole radiation long back by Michel & Goldwire (1970) and Davis & Goldstein (1970). Then the quadrupolar radiation was included in the calculation along with the dipole radiation (Chau & Henriksen 1970). The equations were generalized by Melatos (2000) for non-axisymmetric stars because magnetic field and rotation actually deform the star. Also, this formalism has been used to describe the highly magnetized NSs known as magnetars (Lü et al. 2018; Şaşmaz Muş et al. 2019; Lander & Jones 2020). Kalita et al. (2020) calculated the decay timescales due to dipole and GW radiation for WDs.

Nevertheless, the viscous effect of NS matter may try to increase the obliquity angle by redistributing angular momentum. This may turn the NS into an orthogonal rotator, i.e. obliquity angle 90° , if the NS is toroidal magnetic field dominated. The early evolution of the obliquity angle depends on the relative strength between dipole/quadrupole radiations and viscous damping. If the viscous damping is dominating for a particular star/model, the star will be able to radiate GW for the longer time (Cutler 2002; Dall’Osso et al. 2009).

However, the magnetic field also decays due to Ohmic dissipation, ambipolar diffusion, and Hall drift (Goldreich & Reisenegger 1992; Heyl & Kulkarni 1998), shown for magnetar. Each of these processes may dominate the decay depending on the magnetic field strength. Mondal (2021) studied spin-down and magnetic field decay for NSs to measure the age of present-day magnetars. Interestingly, Bhattacharya et al. (2022) studied magnetic field decay for WDs to argue that super-Chandrasekhar WDs born as a result of strong-field effects may not remain so forever.

It is important to note that pulsating highly magnetized NSs may not radiate GW for very long. Due to decays mentioned above, after some time, either the magnetic and rotation axes align with each other, or they stop rotating, thus do not behave as pulsar anymore. Also, the magnetic field decays, so the ellipticity does, hence the GW radiation also decreases. Therefore, it is necessary to study the timescale for which the NS will be detectable by GW. This exploration will also suggest that the detection of NS by its CGW may be challenging, depending on the decays of various parameters.

We plan to study the plausible instantaneous GW detection from isolated NSs by some upcoming detectors. At present, immense effort is going on to increase the sensitivity of GW detectors for various sources (Sieniawska & Bejger 2019), which can be done by improving the signal-to-noise ratio (SNR) of detector. However, by calculating SNR for certain integrated time, we can detect GW from a source which could not be detected instantaneously. Thereby we can estimate the necessary observation time for the particular GW detector to detect these objects before their radiation decays away.

To radiate electromagnetic dipole radiation, the NS should have a certain amount of poloidal magnetic field (Sousa et al. 2020). However, Wickramasinghe et al. (2014) argued that the NS should be eventually toroidally dominated due to the action of Ω -dynamo. Therefore, in this work, we calculate the SNR of GW signal considering toroidally dominated NSs. Nevertheless, we will show some results for the poloidally dominated counterpart for completeness. Highly magnetized NSs or magnetars are most probably the remnants of core-

collapse supernova, which may also be hypermassive due to differential rotation acquired at their birth (Shibata & Uryū 2000; Zwerger & Mueller 1997; Rampp et al. 1998). However, in the Alfvén timescale, the differentially rotating NS is expected to rapidly settle into a uniformly rotating, less massive NS due to magnetic braking (Shapiro 2000; Cook et al. 2003; Liu & Shapiro 2003). Note that dynamo driven by differential rotation may also be the source of the strong magnetic field of magnetar (Wickramasinghe et al. 2014).

In this paper, we show that rotating, magnetized NSs with softer EoS can produce massive NSs, sometimes with $M > 2M_{\odot}$, some of which will be detectable by upcoming detectors. We argue that the non-detection of those NSs will put an upper bound on ellipticity and thus magnetic field. However, as mentioned above, those pulsating magnetized NSs may not behave like pulsars for a very long time or become less massive due to various decay mechanisms. Therefore, we calculate the underlying timescales and also show how GW strain decays. Further we calculate the corresponding SNR to detect such objects by various GW detectors in one year of integration time. The plan of the paper is as follows. In Section 2, we discuss the model of the pulsating, magnetized compact object radiating GW. Next, in Section 3, we discuss our results for NSs considering various central densities and magnetic field geometries with the change of angular frequency. In Section 4, we discuss how GW amplitude decreases due to magnetic field decay. The next part, Section 5, is to discuss the timescales of various pulsating NSs behaving as pulsars and show how GW amplitude decays with time. For the completeness of discussions of various decay channels, Section 6 explores the viscous and thermal effects in controlling the pulsations. In Section 7, we calculate corresponding SNR for poloidally and toroidally dominated NSs and discuss the timescales for detecting them. In Section 8 we calculate the Alfvén timescale in which NSs become less massive due to magnetic braking. Finally we end with conclusions in Section 9.

2 MODELLING GRAVITATIONAL WAVES FROM PULSATING COMPACT STARS

It has already been shown that to emit CGW, a compact star must have non-zero obliquity angle (Bonazzola & Gourgoulhon 1996). Fig. 1 shows a cartoon diagram of a pulsar with z' being the rotation axis and z the magnetic field axis, where the angle between these two axes is χ (obliquity angle). The magnetic field, as well as rotation, deforms the shape and changes the size of any star (Cutler 2002; Ioka & Sasaki 2004; Kiuchi & Yoshida 2008; Mastrano et al. 2015; Subramanian & Mukhopadhyay 2015; Suvorov et al. 2016). The toroidal magnetic field deforms a star into a prolate shape and enlarges its size, whereas the poloidal magnetic field compels a star to oblate shape and reduces its size. The effects of rotation act in a similar way as of poloidal field, except that the former increases the equatorial radius of the star due to the centrifugal force (Cutler 2002; Ioka & Sasaki 2004; Kiuchi & Yoshida 2008; Friebe & Rezzolla 2012; Mastrano et al. 2015; Subramanian & Mukhopadhyay 2015; Suvorov et al. 2016; Kalita & Mukhopadhyay 2019). If the magnetic field and rotation are present simultaneously, with misalignment between their respective axes, they comprehensively make the star triaxial,

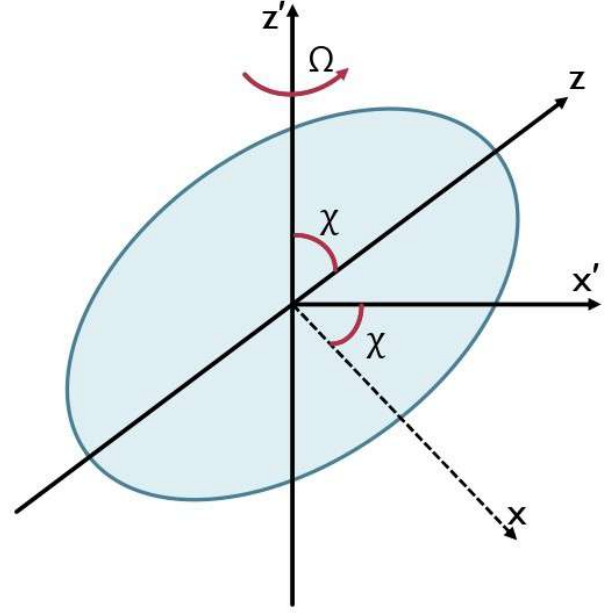


Figure 1. A cartoon diagram of magnetized rotating compact star with misalignment between the magnetic field axis and rotation axis.

which can produce dipole as well as gravitational radiations. The strain of the two polarizations of the GW at any time t is given by (Bonazzola & Gourgoulhon 1996; Zimmermann & Szedenits 1979)

$$\begin{aligned} h_+ &= h_0 \sin \chi \left[\frac{1}{2} \cos i \sin i \cos \chi \cos \Omega t - \frac{1 + \cos^2 i}{2} \sin \chi \cos 2\Omega t \right], \\ h_{\times} &= h_0 \sin \chi \left[\frac{1}{2} \sin i \cos \chi \sin \Omega t - \cos i \sin \chi \sin 2\Omega t \right]. \end{aligned} \quad (1)$$

Here,

$$h_0 = \frac{2G}{c^4} \frac{\Omega^2 \epsilon I_{xx}}{d} (2 \cos^2 \chi - \sin^2 \chi), \quad (2)$$

for $\chi \rightarrow 0$ (but $\neq 0$),

$$h_0 = \frac{4G}{c^4} \frac{\Omega^2 \epsilon I_{xx}}{d}, \quad (3)$$

where c is the speed of light, G is Newton’s gravitational constant, Ω is the angular frequency of the object, d is the distance between the detector and the source object, i is the angle between the rotation axis of the object and our line of sight, and ellipticity is defined as $\epsilon = |I_{zz} - I_{xx}|/I_{xx}$, where I_{xx} and I_{zz} are the principal moments of inertia of the star about x - and z -axes, respectively. An object behaving as a pulsar can emit CGWs at two frequencies, Ω and 2Ω .

To calculate the quantities such as I_{xx} , I_{zz} , etc., we use the *XNS* code¹, a numerical code to solve the structure of

¹ <https://www.arcetri.inaf.it/science/ahead/XNS/code.html>

NSs in general relativity (Pili et al. 2014). This code, however, solves only for the axisymmetric equilibrium configuration of stellar structure, with rotation (uniform or differential) and/or magnetic field (toroidal or poloidal or mixed field). Hence, the code implicitly assumes the magnetic and rotation axes to be aligned or marginally misaligned. Otherwise, the code solves the time-independent general relativistic magnetostatic equations. Hence, the star might not be in the stable equilibrium purely based on the *XNS* results because the code generates the equilibrium structure of a star even in the presence of a very high magnetic field, which might be unstable from the stability analysis, particularly for purely toroidal or poloidal field configurations (Wright 1973; Tayler 1973; Markey & Tayler 1974; Tayler 1980; Braithwaite 2006, 2007; Lander & Jones 2012; Lander 2013; Ciolfi & Rezzolla 2013). To assure stability of a NS, the ratio of magnetic to gravitational energies (ME/GE) to be $\lesssim 10^{-3}$ (Komatsu et al. 1989; Braithwaite 2009; Akgün et al. 2013; Herbrink & Kokkotas 2017). However, this limit may be eased up by building a suitable configuration with a mixed field, which turns out to be toroidally dominated (Wickramasinghe et al. 2014). Nevertheless, our current endeavour is not to study the stability analysis but instead to explore the detectability of GW from NSs with given magnetic field strengths. As the *XNS* code does not have, as of now, a provision of a rotating star with appropriate (i.e. toroidally dominated) and/or an equal fraction of mixed field configuration, it can deal with only poloidally dominated mixed field configuration (twisted torus). Therefore, purely poloidal or purely toroidal magnetic fields, maintaining the ME/GE limit given by Braithwaite (2009) mentioned above, should be a valid approximation for poloidally dominated or toroidally dominated mixed field configurations, respectively.

For the solution of a NS, we need to supply the EoS. However, the *XNS* code requires EoS in the polytropic form, i.e., $\mathcal{P} = K\rho^\Gamma$ with \mathcal{P} being the pressure, ρ the density, Γ is the polytropic index, and K is the polytropic constant. However, the exact EoS of NSs is not well established. Pili et al. (2014) assumed $\Gamma = 2$ and $K = 1.45 \times 10^5 \text{ cm}^5 \text{ g}^{-1} \text{ s}^{-2}$. From the concept of tidal deformability, EoS however can be constrained from the observation of GW emission (Abbott et al. 2017d, 2018, 2019a) detected by the LIGO/Virgo Collaboration. Based on this, Chatziioannou (2020) and Deb et al. (2021) argued that Γ should not be ≥ 2 and EoS to be a bit softer. Therefore, we will choose $\gamma = 1.95$, $K = 11.3 \times 10^5 \text{ cm}^5 \text{ g}^{-1} \text{ s}^{-2}$ for this work. Furthermore, if one fits the data of actual EoS with the polytropic law, most are well fitted with the polytropic index $\sim 1.8 - 2.2$. Hence, our choice is justified. Indeed it is known that EoS in polytropic form appropriately captures ellipticity of NSs as it does for realistic EoS (Gualtieri et al. 2011). We choose maximum central density $\rho_c = 10^{15} \text{ g cm}^{-3}$ for NS, because above this ρ_c , quarks may be produced at the centre due to phase transition, making it a hybrid star.

Moreover, the code implicitly assumes χ to be zero (or does not include information about χ). However, if there is no misalignment between magnetic field and rotation axes, the star does not radiate GW radiation. Hence, we make small χ approximation in our computations related to CGW based on the *XNS* outputs to avoid the ambiguity in the structure of the object. However, if we could run an efficient code with appropriately chosen χ , we should be able to generate much

higher GW strain as it increases with the angle χ . This implies that we can use equation (3) effectively. Further, the amplitudes of h_+ and h_\times in equation (1) will be suppressed by the other factors present therein. For instance, at $\chi = 3^\circ$,

$$\max \left(\sin \chi \left[\frac{1}{2} \cos i \sin i \cos \chi \cos \Omega t - \frac{1 + \cos^2 i}{2} \sin \chi \cos 2\Omega t \right] \right) = 0.0110297 \quad (4)$$

for $t = 0$ and $i = i_{\max} \approx 46.5^\circ$. Hence, maximum amplitude received by the detector at $\chi = 3^\circ$ is $h = 0.0110297 h_0$, which we consider for further calculations. Further, we assume the distance between the NS and the detector to be 10 kpc. Importantly, only the ellipticity arising due to magnetic field, but not from rotation, is responsible for CGW; hence one has to switch off the rotational effect to extract ellipticity from the run of *XNS* code.

3 CONTINUOUS GRAVITATIONAL WAVE AMPLITUDE FROM MASSIVE NEUTRON STARS

We consider purely toroidal and purely poloidal magnetic field cases separately for different EoSs, i.e., with various Γ . In reality, NSs are expected to be consisting of mixed field geometry. Thus, the actual results might be in between that of purely poloidal and purely toroidal configurations. Kalita & Mukhopadhyay (2019) initiated the variation of h_0 for NSs with the change of ρ_c , Ω and magnetic field. Here we explore h_0 in order to detect massive NSs and the role of EoS parameters in it.

3.1 Neutron stars with purely toroidal magnetic field

It was already known that a purely toroidal magnetic field deforms the NS into a prolate shape and increases its size (Pili et al. 2014; Kalita & Mukhopadhyay 2019), as seen in Fig. 2. It is observed that the deformation due to the magnetic field at the core is more prominent than in the outer region. However, the rotation makes it oblate; consequently, there is a competition between these two opposing effects to decide the overall shape of the star. In the inner region, the star will be more of a prolate shape because the magnetic field effect dominates near the core. In outer layers, where the magnetic field decreases and centrifugal term ($\propto r$ for uniform rotation) becomes large, the shape becomes oblate. For smaller magnetic field with ME/GE $\lesssim 10^{-3}$ there is practically no deviation of shape from spherical symmetry.

Table 1 shows h_0 for various uniformly rotating NSs with different ρ_c and magnetic fields B for $\Gamma = 1.95$. In the table, R_E the equatorial radius of NS, R_P the polar radius, and ν the linear frequency defined as $\nu = \Omega/2\pi$. For larger B , the NS deviates more from spherical geometry, which produces higher quadrupole moment and, thus, higher ellipticity. Since $h_0 \propto \epsilon$, this leads to increasing h_0 . M also increases with B because the star will be able to hold more mass due to increased outward magnetic pressure (but see Deb et al. 2021). We consider different frequencies with high ME/GE, as well as low ME/GE ($\leq 10^{-3}$). It shows that NSs with high

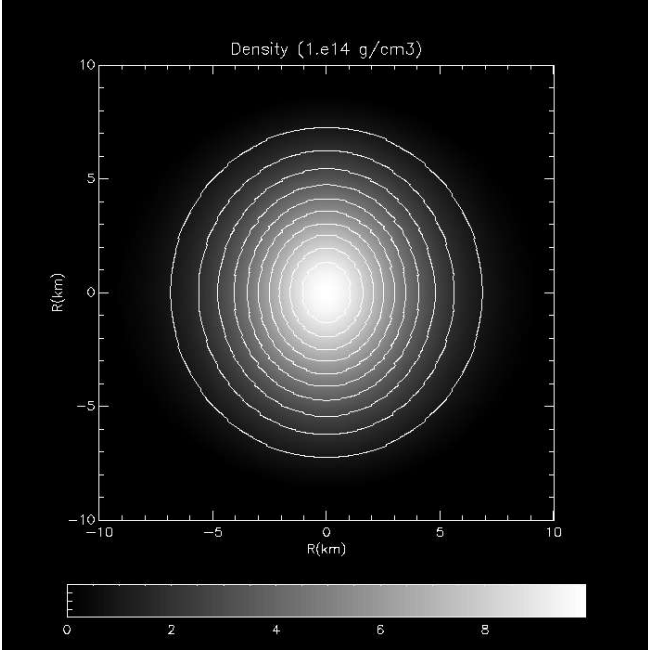


Figure 2. Density isocontours of uniformly rotating toroidally magnetized NS of mass $M = 1.97M_{\odot}$ with $\nu = 500$ Hz, $B_{max} = 4.5 \times 10^{17}$ G, ME/GE = 5.6×10^{-2} and KE/GE = 2.3×10^{-2} .

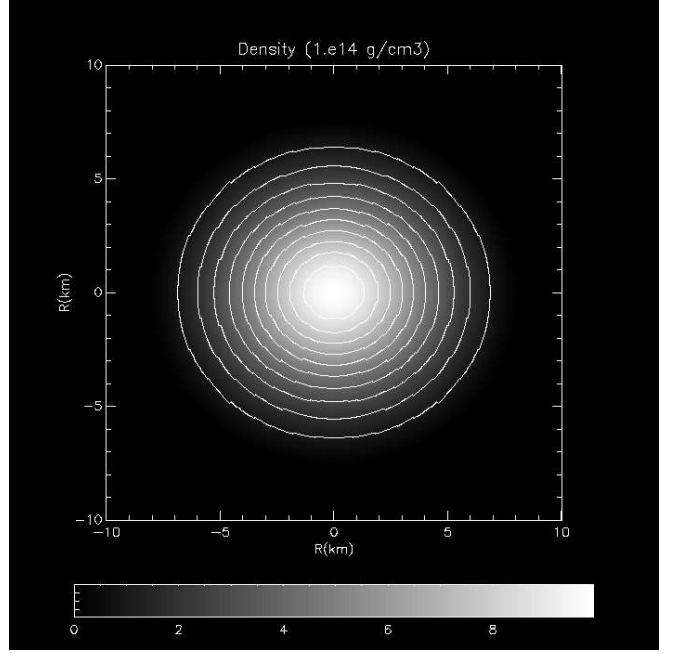


Figure 3. Density isocontours of uniformly rotating poloidally magnetized NS of mass $M = 1.92M_{\odot}$ with $\nu = 50$ Hz, $B_{max} = 4.4 \times 10^{17}$ G, ME/GE = 2×10^{-2} and KE/GE = 2×10^{-4} .

ME/GE emit GW more efficiently. From Tables 1 and 2 (will be discussed below), it is also clear that highly magnetized NSs are indeed massive, sometimes with $M > 2M_{\odot}$.

3.2 Neutron stars with purely poloidal magnetic field

A similar exploration is carried out for uniformly rotating NSs with a purely poloidal magnetic field. Purely poloidal magnetic field and rotation both affect the star similarly, deforming it into an oblate shape, as shown in Fig. 3. Table 2 shows h_0 for various NSs.

3.3 Neutron stars with different polytropic index

We choose different Γ with the same toroidal magnetic field in the core to see how M and h_0 change with EoS. From Table 3, it is clear that a more massive NS is achievable with softer EoSs, however steeper EoSs lead to more compact stars. Nevertheless, the effect of EoS on ellipticity is very small.

All the values of h_0 presented in Tables 1-3 are displayed in Figs. 4 and 5, along with the various sensitivity curves of different detectors. From equation (1), we know that if χ is larger, the gravitational radiation will be more efficient. Interestingly there has been no detection of CGW from NSs in LIGO, VIRGO, aLIGO, and aVIRGO so far (Abbott et al. 2019b,c; Piccinni et al. 2020). Hence, we can interpret that they are so hard to detect because the GW strain decays due to, e.g., magnetic field decay and spin-down (will be discussed in Sections 4 and 5). If any of them is detected in the future by Einstein Telescope, Cosmic Explorer, etc., depending on their distance from the Earth, the magnetic field can be predicted from ellipticity. The detection of CGWs from isolated

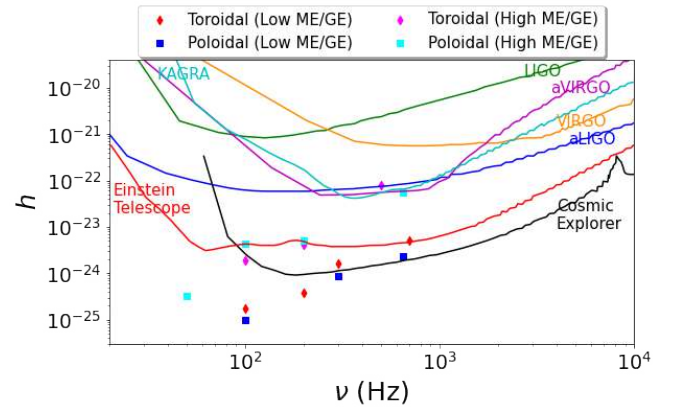


Figure 4. Dimensionless gravitational wave amplitude for NSs as a function of frequency, as given in Tables 1-2, along with the sensitivity curves of various detectors. Here $h = 0.0110297h_0$ with $\chi = 3^\circ$.

NS would be a fundamental breakthrough, which can provide us an idea about its spin, magnetic field, as well as the nuclear and particle constituents of inner structure from EoS parameters. However, from the non-detection of CGW from NSs, we can obtain the maximum deformation supported by the NS, i.e., the upper limit of ellipticity and thus the maximum magnetic field sustained by it (Abbott et al. 2019b; Maggiore et al. 2020; Dergachev & Papa 2021).

Table 1. Uniformly rotating NS with toroidal magnetic field for $\chi = 3^\circ$. Here B_{max} is the maximum magnetic field when the surface field could be much smaller.

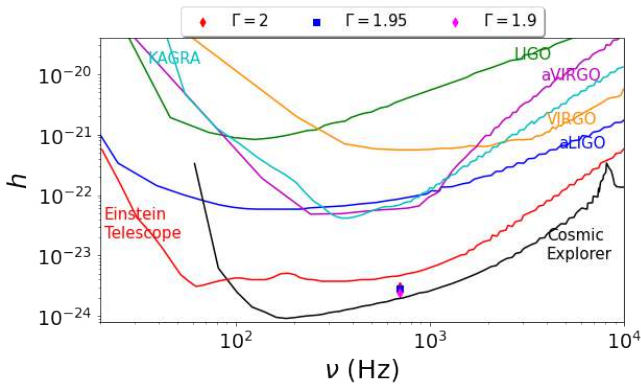
ρ_c (g/cc)	M (M_\odot)	R_E (km)	R_P/R_E	B_{max} (G)	ν (Hz)	ME/GE	KE/GE	$ \epsilon $	h_0 ($d = 10$ kpc)
10^{15}	1.97	13.97	0.92	4.5×10^{17}	500	5.6×10^{-2}	2.3×10^{-2}	0.11	7.3×10^{-21}
10^{15}	1.91	12.48	0.986	2.8×10^{17}	200	2×10^{-2}	3×10^{-3}	0.11	3.7×10^{-22}
10^{15}	1.908	11.99	0.99	9×10^{16}	200	2×10^{-3}	3×10^{-3}	4×10^{-3}	3.5×10^{-23}
10^{15}	2.039	13.31	0.81	9×10^{16}	700	2.1×10^{-3}	4.2×10^{-2}	4×10^{-3}	4.5×10^{-22}
5×10^{14}	1.64	15.8	0.97	1.5×10^{17}	100	2×10^{-2}	2.3×10^{-3}	0.039	1.7×10^{-22}
5×10^{14}	1.638	15.3	0.99	4.5×10^{16}	100	1.5×10^{-3}	1.6×10^{-3}	3.9×10^{-3}	1.6×10^{-23}
5×10^{14}	1.68	15.63	0.94	4.5×10^{16}	300	2.8×10^{-4}	1.5×10^{-2}	3.9×10^{-3}	1.5×10^{-22}

Table 2. Uniformly rotating NS with poloidal magnetic field and $\chi = 3^\circ$. Here B_{max} is the maximum magnetic field at the centre, when the surface field could be much smaller.

ρ_c (g/cc)	M (M_\odot)	R_E (km)	R_P/R_E	B_{max} (G)	ν (Hz)	ME/GE	KE/GE	$ \epsilon $	h_0 ($d = 10$ kpc)
10^{15}	2.045	12.82	0.81	4.4×10^{17}	650	2.2×10^{-2}	3.7×10^{-2}	0.058	5.1×10^{-21}
10^{15}	1.93	11.99	0.946	4.4×10^{17}	200	2×10^{-2}	3×10^{-3}	0.058	4.7×10^{-22}
10^{15}	1.921	11.99	0.945	4.4×10^{17}	50	2×10^{-2}	2×10^{-4}	0.058	3×10^{-23}
10^{15}	2.017	12.98	0.85	9×10^{16}	650	9×10^{-4}	3.7×10^{-2}	2.2×10^{-3}	2.1×10^{-22}
5×10^{14}	1.69	15.3	0.91	3×10^{17}	100	3×10^{-2}	1.6×10^{-3}	9×10^{-2}	4×10^{-22}
5×10^{14}	1.64	15.2	0.98	4.5×10^{16}	100	5.7×10^{-4}	1.6×10^{-3}	2.1×10^{-3}	9×10^{-24}
5×10^{14}	1.68	15.5	0.94	4.5×10^{16}	300	6.1×10^{-4}	1.5×10^{-3}	2.1×10^{-3}	8×10^{-23}

Table 3. Uniformly rotating toroidally magnetized NS with varying polytropic index Γ and $\chi = 3^\circ$. Here B_{max} is the maximum magnetic field when the surface field could be much smaller.

Γ	ρ_c (g/cc)	M (M_\odot)	R_E (km)	R_P/R_E	B_{max} (G)	ν (Hz)	ME/GE	KE/GE	h_0 ($d = 10$ kpc)
2.0	10^{15}	1.62	12.156	0.823	6.1×10^{16}	700	1×10^{-3}	4.3×10^{-2}	2.8×10^{-22}
1.95	10^{15}	2.039	13.31	0.814	6×10^{16}	700	8.7×10^{-4}	4.4×10^{-2}	2.6×10^{-22}
1.9	10^{15}	2.457	14.64	0.8	5.9×10^{16}	700	7×10^{-4}	4.5×10^{-2}	2.2×10^{-22}

**Figure 5.** Dimensionless gravitational wave amplitude for NSs as a function of frequency, as given in Table 3, along with the sensitivity curves of various detectors. Here $h = 0.0110297h_0$ with $\chi = 3^\circ$.

4 MAGNETIC FIELD DECAY

In a strongly magnetized NS Ohmic decay, ambipolar diffusion, and Hall drift are the origin of the magnetic energy release. Each of these processes may dominate the evolution depending on the magnetic field strength and the density of the NS. However, even though the magnetic fields throughout the NS decay by all three mechanisms, dissipation due to ambipolar diffusion may dominate given its plausible higher field.

The timescales for Ohmic, ambipolar, and Hall effects, given by Heyl & Kulkarni (1998), are respectively,

$$t_{ohmic} \sim 2 \times 10^{11} \frac{L_5^2}{T_8^2} \left(\frac{\rho}{\rho_{nuc}} \right)^3 \text{ yr}, \quad (5)$$

$$t_{ambipolar} \sim \frac{5 \times 10^{15}}{T_8^6 B_{12}^2} \text{ yr} + t_{ambipolar}^s, \quad (6)$$

where

$$t_{ambipolar}^s \sim 3 \times 10^9 \frac{L_5^2 T_8^2}{B_{12}^2} \text{ yr}, \quad (7)$$

and

$$t_{Hall} \sim 5 \times 10^8 \frac{L_5^2 T_8^2}{B_{12}} \left(\frac{\rho}{\rho_{nuc}} \right) \text{ yr}, \quad (8)$$

where L_5 is the characteristic length scale of the flux loops through the outer core in units of 10^5 cm, T_8 is the core temperature in units of 10^8 K, and B_{12} is the magnetic field strength in units 10^{12} G. Ohmic decay dominates in the weak field limit ($B \lesssim 10^{11}$ G), fields of medium strength ($B \sim 10^{12} - 10^{13}$ G) is dissipated via Hall drift, and very strong fields ($B \gtrsim 10^{14}$ G) strongly decay by ambipolar diffusion. For details on the operation of the decay mechanism, see Heyl & Kulkarni 1998.

The magnetic field decay in NSs can be studied, following Heyl & Kulkarni (1998), by solving the decay equation,

$$\frac{dB}{dt} = -B \left(\frac{1}{t_{ohmic}} + \frac{1}{t_{ambipolar}} + \frac{1}{t_{Hall}} \right). \quad (9)$$

By solving equation (9) through the star, we obtain the decay of the magnetic field profile throughout NS. The initial magnetic field profile is taken from the *XNS* output data.

It is evident from the density and field dependent expressions for the above mentioned timescales that although Hall and Ohmic can occur throughout the star, at the core they will be suppressed by ambipolar diffusion, which only happens in core (Goldreich & Reisenegger 1992). Thus the magnetic field decay given by equation 9 in the core will be governed by ambipolar diffusion.

The Hall and Ohmic effects do not work practically in the core, as the ambipolar takes over therein. However, ambipolar diffusion, which can be divided into solenoidal and irrotational component, may be suppressed due to appearance of hyperons above certain density and superconductivity below certain temperature while NS cooling (Baym et al. 1969; Colpi et al. 1999; Glampedakis et al. 2011). Thus, it has been suggested that magnetic field decay is governed by Hall drift and ohmic dissipation at the crust (Yakovlev & Urpin 1980; Pons et al. 2009). Nevertheless, a field $> 5 \times 10^{16}$ G would void superconducting activity (Tilley et al. 2019) and the field in $10^{15} - 5 \times 10^{16}$ G (Sinha & Sedrakian 2015) would make superconducting effect weak. Therefore, even the ambipolar effect might remain to be unaffected or weakly affected (Dall’Osso et al. 2009).

4.1 Neutron stars with purely toroidal magnetic field

We start with an initial uniformly rotating NS model based on *XNS* with $\Gamma = 1.95$ and $\rho_c = 10^{15}$ g cm $^{-3}$. Substituting *XNS* output in equation (9) as the initial condition, we obtain the field profile as a function of time. Fig. 6 shows the magnetic field profiles in a NS at different ages. For the maximum magnetic field of the star, Fig. 7 shows how the field decays with time. After certain time, we can estimate B_{max} from Fig. 7 and can model another NS with such a B_{max} . Fig. 9 shows how the GW amplitude decays with time as B decays, assuming Ω and χ fixed. As seen in the figure, initially, NS could be detected by the Einstein Telescope and Cosmic Explorer, however, after a certain time, it will be undetectable. In Fig. 6, all the magnetic field profiles are shown assuming same radius for the NS. Nevertheless, with decreasing B , the

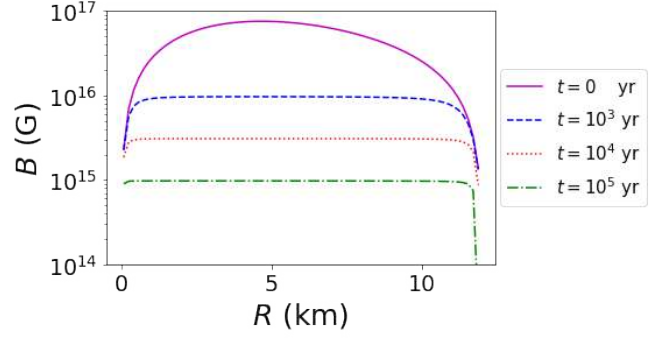


Figure 6. Magnetic field as a function of radius, before and after magnetic field decay, as given in Table 4 for toroidal field.

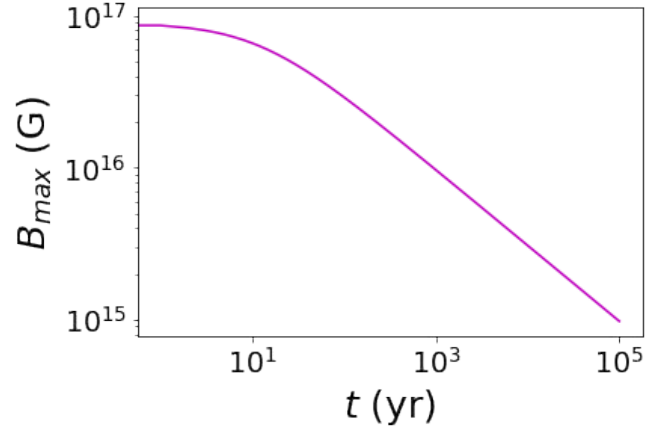


Figure 7. Maximum magnetic field as a function of time of a NS, as given in Table 4 for toroidal field.

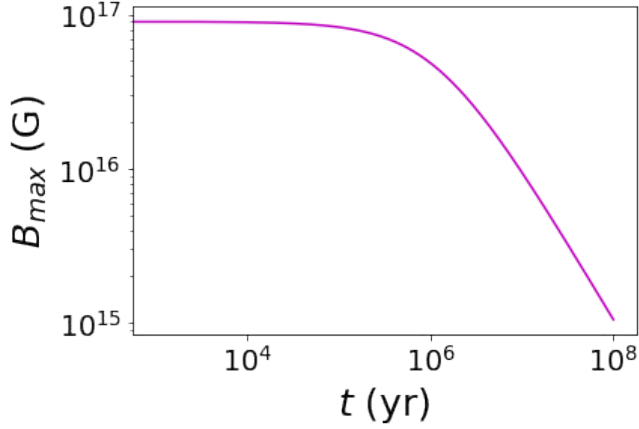
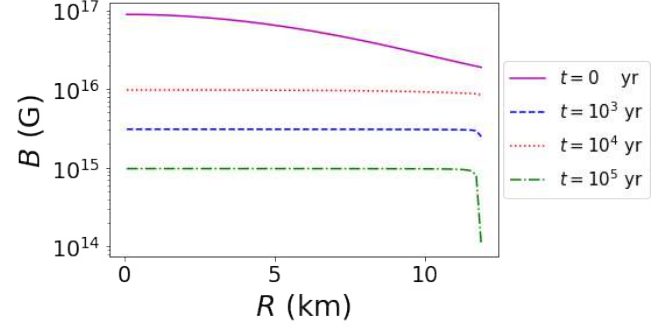
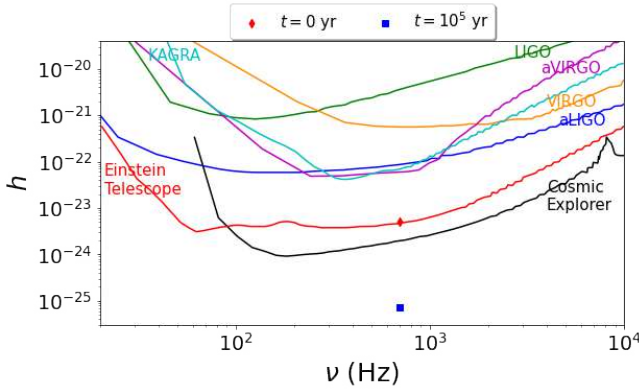
radius of NS should decrease because the outward magnetic pressure decreases. However, for the present case, the change of radius is very negligible (one can look at Table 4), hence the assumption is valid.

If the superconducting effects suppress the ambipolar effect, i.e. if the decay due to ambipolar diffusion does not work, the field decay in the core would slow down, allowing the star to emit GW for a longer time. While the ambipolar effect decreases the core field $\sim 10^{17}$ G to $\sim 10^{15}$ G in 10^5 yr, as shown in Figs. 6 and 7, without it (e.g. by means of Hall and Ohmic effects, which work very slowly at the core density and field) the similar decay requires 10^8 yr, as depicted in Fig. 8.

Nevertheless, note that with time, Ω and χ may decrease significantly. Hence, the GW amplitude at $t > 0$ presented in Table 4 and Fig. 9 need not be accurate. The decays of Ω and χ and their effects on GW amplitude will be discussed in detail in Section 5.

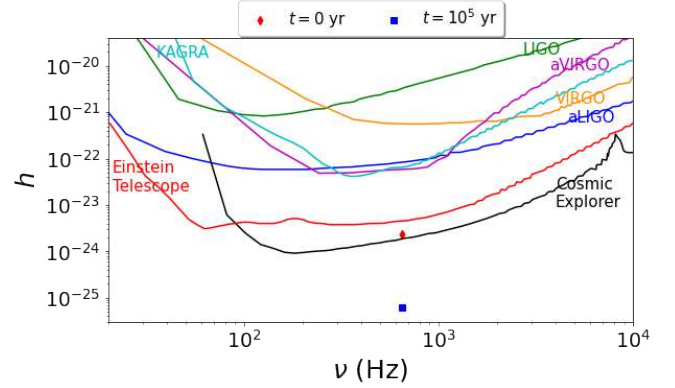
Table 4. Uniformly rotating NS with the toroidal magnetic field at different times after birth, where $\rho_c = 10^{15} \text{ g cm}^{-3}$.

$t(\text{yr})$	$M (M_\odot)$	$R_E (\text{km})$	R_P/R_E	$B_{\text{max}} (\text{G})$	$\nu (\text{Hz})$	ME/GE	KE/GE	$ \epsilon $	$h_0 (d = 10 \text{ kpc})$
0	2.039	13.31	0.81	9×10^{16}	700	2.1×10^{-3}	4.2×10^{-2}	5.1×10^{-4}	4.5×10^{-22}
10^5	2.039	13.15	0.82	10^{15}	700	2×10^{-7}	4.3×10^{-2}	6.2×10^{-5}	6.5×10^{-24}

**Figure 8.** Maximum magnetic field as a function of time of a NS, as given in Table 4 for toroidal field if ambipolar decay is suppressed.**Figure 10.** Magnetic field as a function of radius, before and after magnetic field decay, as given in Table 5 for poloidal fields.**Figure 9.** Dimensionless gravitational wave amplitude for NSs before and after magnetic field decay, as given in Table 4 for toroidal fields. Here $h = 0.0110297h_0$ with $\chi = 3^\circ$.

4.2 Neutron stars with purely poloidal magnetic field

A similar exploration as in Section 4.1 is carried out for a uniformly rotating NS with a purely poloidal magnetic field. The magnetic field profiles after a certain age of the star are shown in Fig. 10. Further, Fig. 11 shows that the GW amplitude decays with time as B decays, provided Ω and χ

**Figure 11.** Dimensionless gravitational wave amplitude for NSs before and after magnetic field decay, as given in Table 5 for poloidal fields. Here $h = 0.0110297h_0$ with $\chi = 3^\circ$.

are fixed (which need not necessarily be true, as mentioned above). See Section 5 below.

5 SPIN-DOWN AND TIME EVOLUTION OF OBLIQUITY ANGLE

A triaxial pulsating NS can simultaneously emit dipole and gravitational radiations, which are incorporated with the dipole and quadrupolar luminosities. The dipole luminosity

Table 5. Uniformly rotating NS with the poloidal magnetic field at different times after birth, where $\rho_c = 10^{15} \text{ g cm}^{-3}$.

$t(\text{yr})$	$M (M_\odot)$	$R_E (\text{km})$	R_P/R_E	$B_{max} (\text{G})$	$\nu (\text{Hz})$	ME/GE	KE/GE	$ \epsilon $	$h_0 (d = 10 \text{ kpc})$
0	2.017	12.98	0.847	9×10^{16}	650	9×10^{-3}	3.7×10^{-2}	5.4×10^{-4}	2.1×10^{-22}
10^5	2.016	12.98	0.847	10^{15}	650	9.7×10^{-8}	3.7×10^{-2}	6.2×10^{-5}	5.6×10^{-24}

for an axisymmetric WD was discussed by Melatos (2000), which is applicable for NS as well, given by

$$L_D = \frac{B_p^2 R_p^6 \Omega^4}{2c^3} \sin^2 \chi F(x_0), \quad (10)$$

where $x_0 = R_0 \Omega / c$, B_p is the strength of the magnetic field at the pole, R_p is polar radius, R_0 is the average radius of NS and the function $F(x_0)$ is defined as

$$F(x_0) = \frac{x_0^4}{5(x_0^6 - 3x_0^4 + 36)} + \frac{1}{3(x_0^2 + 1)}. \quad (11)$$

Similarly, the quadrupolar GW luminosity is given by (Zimmermann & Szedenits 1979)

$$L_{GW} = \frac{2G}{5c^5} (I_{zz} - I_{xx})^2 \Omega^6 \sin^2 \chi (1 + 15 \sin^2 \chi). \quad (12)$$

The rotational frequency of pulsating NS decreases over time due to the extraction of angular momentum by gravitational and electromagnetic dipole radiations, which further leads to changes in obliquity angle, χ . For an oblique rotator, the evolution equations for Ω and χ (for spin-down and alignment) will be involved with a combination of GW radiation and electromagnetic energy-loss terms (Chau & Henriksen 1970; Kalita et al. 2020), given by

$$\frac{d(\Omega I_{z'z'})}{dt} = -\frac{2G}{5c^5} (I_{zz} - I_{xx})^2 \Omega^5 \sin^2 \chi (1 + 15 \sin^2 \chi) - \frac{B_p^2 R_p^6 \Omega^3}{2c^3} \sin^2 \chi F(x_0) \quad (13)$$

and

$$I_{z'z'} \frac{d\chi}{dt} = -\frac{12G}{5c^5} (I_{zz} - I_{xx})^2 \Omega^4 \sin^3 \chi \cos \chi - \frac{B_p^2 R_p^6 \Omega^2}{2c^3} \sin \chi \cos \chi F(x_0), \quad (14)$$

where $I_{z'z'}$ is the principle moment of inertia of the body about the z' -axis. Considering a small χ approximation, it can be written as

$$I_{z'z'} = I_{zz} \cos^2 \chi + I_{xx} \sin^2 \chi. \quad (15)$$

The set of equations (13) and (14) will be solved simultaneously to obtain the timescale over which a NS can radiate or behave like a pulsar. To solve equations (13) and (14), we need to supply the various quantities, such as I_{xx} , I_{zz} , B_p , and R_p at the initial time, which are the output of particular NS model from the XNS code. In the following, we study the evolutions of Ω and χ for various field geometries and their consequences on CGW.

5.1 Neutron stars with purely poloidal magnetic field

We choose $\rho_c = 10^{15} \text{ g cm}^{-3}$, $\Gamma = 1.95$, and various B_p along with the initial $\chi = 3^\circ$, so that we have an idea about the timescales for purely poloidally magnetized NSs behaving as pulsars.

We can treat the NSs as oscillating/rotating dipoles; hence, the dipole luminosity formula is applicable. All the different B_p s are given in Table 6 along with the respective M , R_p , and h_0 at $t = 0$ assuming $d = 10 \text{ kpc}$. We restrict ME/GE to less than 10^{-3} so that the magnetized NSs are surely stable (Komatsu et al. 1989; Braithwaite 2009). Below we discuss the time evolutions of the rotational frequency, χ , and the various luminosities of NSs.

5.1.1 Case I: $L_D \gg L_{GW}$

NSs holding a high magnetic field have $L_D \gg L_{GW}$ because L_D increases with the poloidal magnetic field. Thus, the luminosity is dominated by L_D , while the decay rates of rotation frequency and obliquity angle are proportional to total luminosity; L_D governs the timescale. Furthermore, the total luminosity of the NS decreases with time due to a decrease in χ and/or Ω . When $L_D \gg L_{GW}$, χ decays faster than Ω . Let us denote the timescale for the change of χ from its initial value to 0 be T_χ and the corresponding Ω to saturate be T_Ω . Kalita et al. (2020) calculated the timescales by integrating the equations (13) and (14) approximately, assuming $I_{z'z'}$ is not changing with time. The timescales are given by

$$T_\Omega \sim \left(\frac{2I_{z'z'} c^3}{B_p^2 R_p^6 \Omega^2 F(x_0)} \right) \frac{1}{2 \sin^2 \chi} \quad (16)$$

and

$$T_\chi \sim \left(\frac{2I_{z'z'} c^3}{B_p^2 R_p^6 \Omega^2 F(x_0)} \right) \ln(\cot \chi). \quad (17)$$

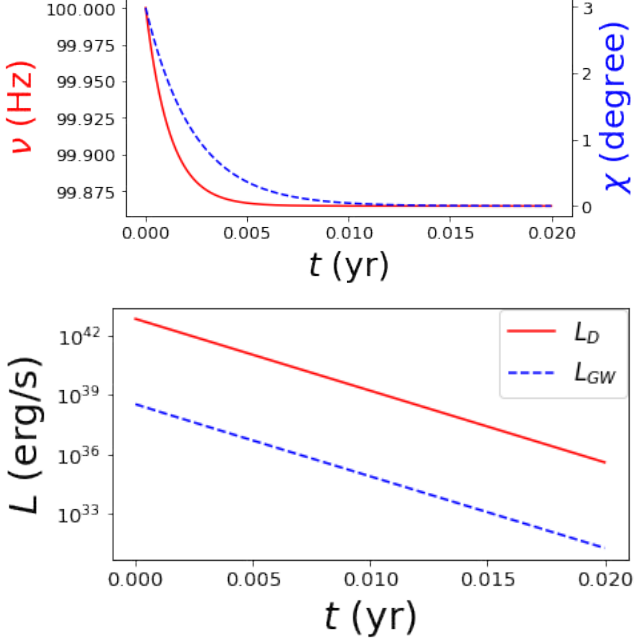
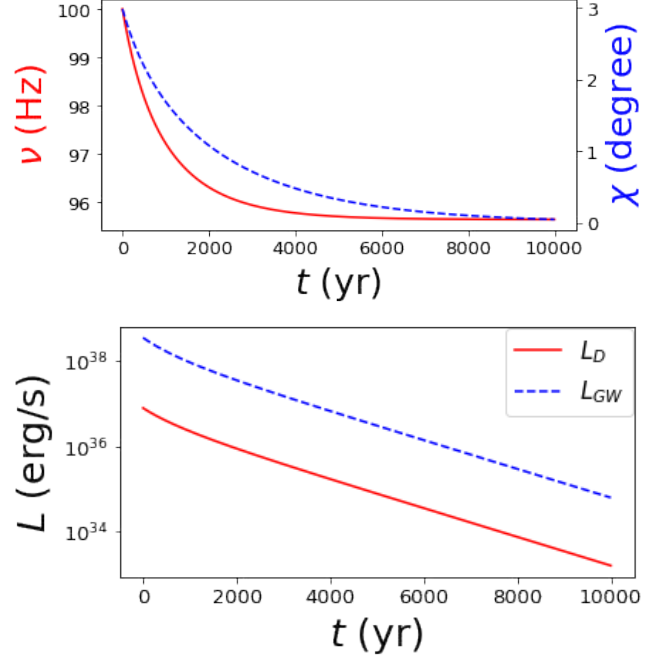
In the range $0^\circ \leq \chi \leq 3^\circ$, we will have $\ln(\cot \chi) \ll 1/2 \sin^2 \chi$, which suggests $T_\chi \ll T_\Omega$. This demonstrates that χ becomes 0 very fast, and the NS starts rotating with a different angular frequency (thus linear frequency) than it originally possesses, which can be seen from Fig. 12, along with the decays of L_D and L_{GW} . For instance, if $M = 1.9 M_\odot$, $B_p = 10^{15} \text{ G}$, $R_p = 12 \text{ km}$, and at $t = 0$, $\nu = 100 \text{ Hz}$ and $\chi = 3^\circ$, such that $L_D \gg L_{GW}$, then $T_\Omega \sim 30 \text{ yr}$ and $T_\chi \sim 0.24 \text{ yr}$, hence $T_\chi \ll T_\Omega$. Due to high L_D , and thus very fast decay of χ and L_D , this NS cannot emit radiation for a long. The future GW detectors may detect such NSs just for a very short duration of time only or may not be able to detect at all.

5.1.2 Case II: $L_{GW} \gg L_D$

If the magnetic field is lower, the NSs may have $L_{GW} \gg L_D$. Then, luminosity decreases slowly, and the NS can radiate

Table 6. Poloidal magnetic field with $\rho_c = 10^{15} \text{ g cm}^{-3}$ and $\nu = 100 \text{ Hz}$. I_{xx} and I_{zz} are in the units $4.5 \times 10^{43} \text{ g cm}^2$.

M (M_\odot)	R_P (km)	B_P (G)	ME/GE	KE/GE	I_{xx}	I_{zz}	L_{GW} (erg/s)	L_D (erg/s)	h_0 ($d = 10 \text{ kpc}$) at $t = 0$	T_Ω (yr)	T_χ (yr)
1.9	11.99	1×10^{15}	4.7×10^{-6}	7.7×10^{-4}	11.41	11.44	3.5×10^{38}	7.7×10^{42}	4.2×10^{-24}	0.45	0.003
1.9	11.99	1×10^{12}	1×10^{-11}	7.7×10^{-4}	11.41	11.44	3.5×10^{38}	7.7×10^{36}	1.3×10^{-25}	439278.4	3507.5

**Figure 12.** $L_D \gg L_{GW}$: Variations of ν , χ , L_{GW} and L_D with time for $B_P = 10^{15} \text{ G}$, initial $\nu = 100 \text{ Hz}$, $\chi = 3^\circ$, as given in Table 6. Red (solid) and blue (dashed) lines show the variations of ν and χ , respectively.**Figure 13.** $L_{GW} \gg L_D$: Variations of ν , χ , L_{GW} and L_D with time for $B_P = 10^{12} \text{ G}$, initial $\nu = 100 \text{ Hz}$, $\chi = 3^\circ$, as given in Table 6. Red (solid) and blue (dashed) lines show the variations of ν and χ , respectively.

for a longer period. For $L_{GW} \gg L_D$, the decay timescales are obtained by integrating equations (13) and (14) (Kalita et al. 2020), given by

$$T'_\Omega \sim \left(\frac{5I_{z'z'}c^5}{2G(I_{zz} - I_{xx})^2\Omega^4} \right) \frac{1}{4\sin^2\chi(1 + 15\sin^2\chi)} \quad (18)$$

and

$$T'_\chi \sim \left(\frac{5I_{z'z'}c^5}{2G(I_{zz} - I_{xx})^2\Omega^4} \right) \frac{1}{12} \left(\frac{1}{\sin^2\chi} + 2\ln\cot\chi \right). \quad (19)$$

In the range, $0^\circ \leq \chi \leq 3^\circ$, Ω , and χ decay simultaneously for a long time before approaching a saturated value and zero, respectively. This also can be verified from Fig. 13. This further allows L_{GW} and L_D to remain higher for longer. The decay of Ω and χ is governed by GW radiation mainly. If $M = 1.9M_\odot$, $B_P = 10^{12} \text{ G}$, $R_P = 12 \text{ km}$, and at $t = 0$, $\nu = 100 \text{ Hz}$ and $\chi = 3^\circ$, such that $L_{GW} \gg L_D$, then $T_\Omega \sim 4.4 \times 10^5 \text{ yr}$ and $T_\chi \sim 3.5 \times 10^3 \text{ yr}$.

5.2 Neutron stars with purely toroidal magnetic field

In the above results, we have simply assumed the NS to be poloidally dominated so that we can effectively use the formula for L_D . Actually, stable NSs consist of a suitable mixture of the toroidal and poloidal components. As XNS cannot handle such configuration, now we consider a few cases of NSs for $\Gamma = 1.95$ and $\rho_c = 10^{15} \text{ g cm}^{-3}$ for purely toroidal magnetic field and drop the contribution from the term L_D , assuming that even if the NS possesses any dipole contribution, its effect is much smaller. As in this configuration $L_{GW} \gg L_D$, such a magnetized massive NS can radiate for a long time. Table 7 shows the timescales, T'_Ω and T'_χ , for various NSs to be active in radiating with a toroidally dominated magnetic field. However, detecting such NSs by the GW detector and the duration of detection depends on the (relative) strengths of the toroidal and poloidal field components. If the stable mixed field configuration is indeed toroidally dominated as suggested by, e.g., Wickramasinghe et al. (2014), that configuration remains stable even after

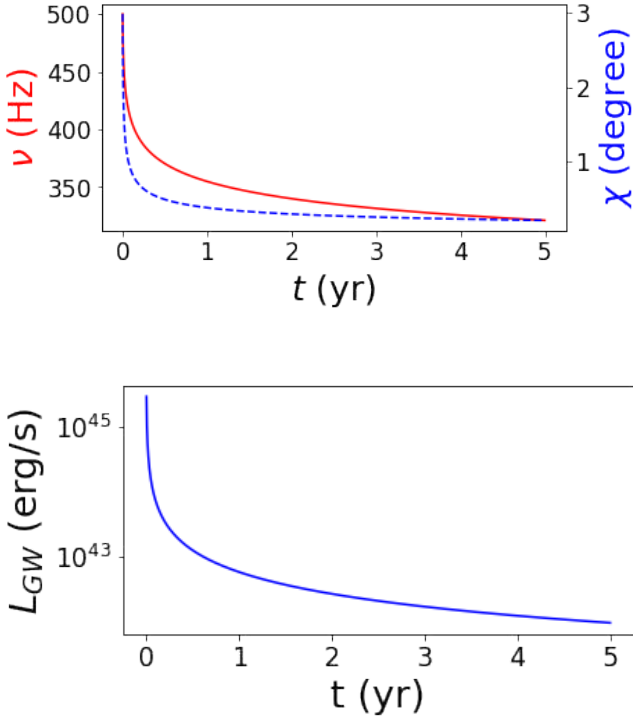


Figure 14. For toroidally dominated NSs, variations of ν , χ and L_{GW} as functions of time for $B_{max} = 1.4 \times 10^{17}$ G, initial $\nu = 500$ Hz, $\chi = 3^\circ$, as given in Table 7. Red (solid) and blue (dashed) lines in the upper panel show the variations of ν and χ , respectively.

a long time, which satisfies the stability criteria given by Braithwaite (2009). Such NSs will be detectable for a longer duration by GW detectors, as implied by Fig. 14 when L_{GW} remains high for a longer duration. The dimensionless GW amplitude for NSs is given in Table 7 at $t = 0$ which, however, will decay with time due to evolutions of Ω and χ . Also, we show in Table 7 that the timescale for NSs behaving as a pulsar increases with smaller Ω (thus smaller ν). Indeed Fig. 15 shows that the change in ν decreases with decreasing initial ν , but T'_Ω and T'_χ increase for smaller initial ν .

Dimensionless gravitational wave amplitude, which is a function of χ and Ω (equations 1 and 3), decays with time as well, as shown in Table 8 and Fig. 16. The dimensionless GW amplitude for NSs at their birth and after some time, along with sensitivity curves of various detectors, have been shown in Fig. 17. As discussed in Sections 4.1 and 4.2, even though the magnetic field remains appreciable at this timescale, due to decays of Ω and χ , the GW amplitude turns out to be much smaller. Also, we can see that the timescale for magnetic field decay is very much larger than the decay timescale of Ω and/or χ ; thus, we consider the magnetic field to be constant during the decay of Ω and χ decay.

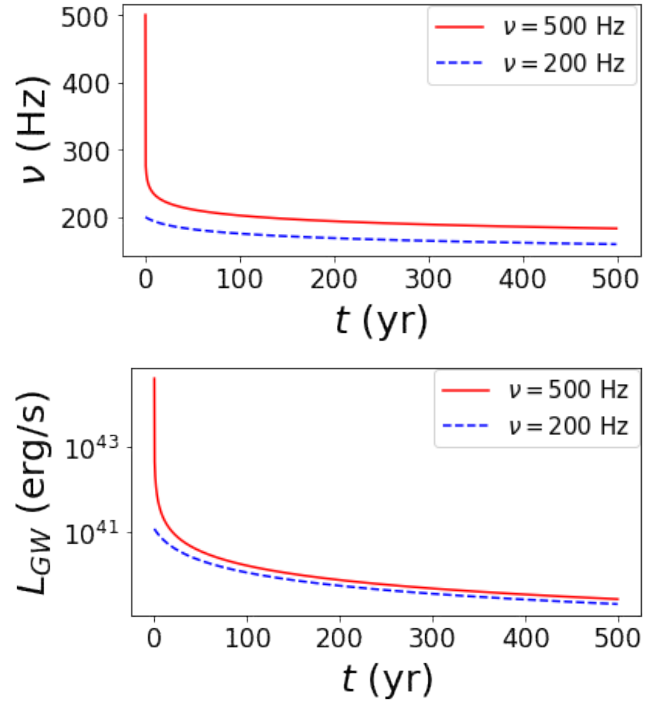


Figure 15. Variations of ν and L_{GW} as functions of time, for different rotation, keeping magnetic field same ($B_{max} = 9 \times 10^{16}$ G).

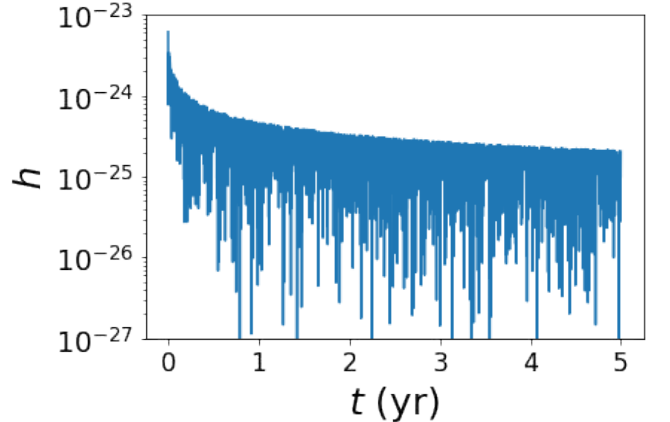


Figure 16. Dimensionless gravitational wave amplitude as a function of time due to decays of Ω and χ (thus h) for $B_{max} = 1.4 \times 10^{17}$ G, initial $\nu = 500$ Hz, $\chi = 3^\circ$, as given in Table 8.

6 VISCOUS AND THERMAL EFFECTS ON OBLIQUITY ANGLE

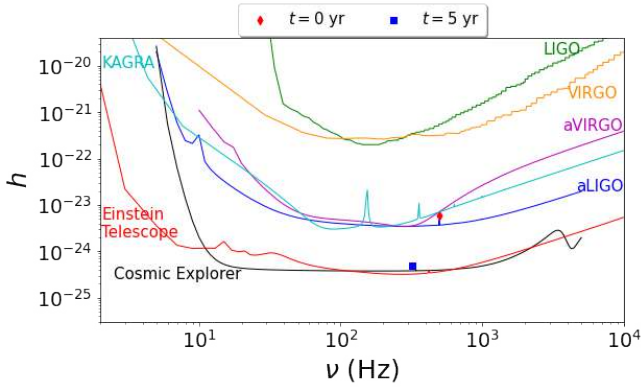
In all the above discussions, we have studied the evolution of obliquity angle due to electromagnetic and GW radiations, both of them extract the angular momentum from the star. As a result, the obliquity angle decreases, leading to the alignment of magnetic and rotating axes of the star. However, in the early days after the formation of NSs before transitioning to superfluidity, the viscous effect may try to

Table 7. Toroidal magnetic field with $\rho_c = 10^{15} \text{ g cm}^{-3}$. I_{xx} and I_{zz} are in the units $4.5 \times 10^{43} \text{ g cm}^2$.

M (M_\odot)	R_E (km)	B_{max} (G)	ν (Hz)	ME/GE	KE/GE	I_{xx}	I_{zz}	L_{GW} (erg/s)	h_0 ($d = 10 \text{ kpc}$) at $t = 0$	T'_Ω (yr)	T'_χ (yr)
1.963	12.65	1.4×10^{17}	500	4.9×10^{-3}	2×10^{-2}	11.53	12.22	2.9×10^{45}	5.6×10^{-22}	0.016	0.006
1.963	12.48	9×10^{16}	500	2×10^{-3}	2×10^{-2}	11.411	11.156	3.9×10^{44}	2.2×10^{-22}	0.1	0.04
1.909	11.99	9×10^{16}	200	2×10^{-3}	3.1×10^{-3}	11.47	11.54	1.2×10^{41}	3.5×10^{-23}	56.5	20.0

Table 8. Change of GW strain (h) for toroidally dominated NS with $\rho_c = 10^{15} \text{ g cm}^{-3}$, $\Gamma = 1.95$, due to Ω and χ decay.

t (yr)	M (M_\odot)	R_E (km)	B_{max} (G)	ν (Hz)	ME/GE	KE/GE	$ \epsilon $	h ($d = 10 \text{ kpc}$)
0	1.963	12.65	1.4×10^{17}	500	4.9×10^{-3}	2×10^{-2}	0.01	6×10^{-24}
5	1.924	12.32	1.4×10^{17}	320	4.8×10^{-3}	8×10^{-3}	0.01	5×10^{-25}

**Figure 17.** Dimensionless gravitational wave amplitude for NSs before and after ν and χ decay along with the sensitivity curve of various detectors for $B_{max} = 1.4 \times 10^{17} \text{ G}$, initial $\nu = 500 \text{ Hz}$, $\chi = 3^\circ$, as given in Table 8.

increase the obliquity angle by redistributing angular momentum. This may turn the NS into an orthogonal rotator, if the NS has a prolate deformation (Cutler 2002) due to toroidally dominated magnetic field. The early evolution of the obliquity angle depends on the relative strength between dipole/quadrupole radiations and viscous damping, which in turn depends on the respective strengths and geometries of the magnetic fields. If the viscous damping is dominating for a particular model, the star will be able to radiate GW for the longer time, which will help them to be detected, as a larger χ leads to higher GW amplitude (Cutler 2002; Dall’Osso et al. 2009).

The viscous effect arises due to bulk viscosity, as the shear viscosity effect is negligible in NS in order to affect χ . The bulk viscosity effect arises due to departure from chemical equilibrium when the matter is compressed and expanded due to the perturbation by Urca processes (Landau & Lifshitz 1987; Lindblom & Owen 2002), the corresponding timescale is given by (Lander & Jones 2018)

$$T_{bulk} = 7.9s \left(\frac{M}{1.4M_\odot} \right)^{5/3} \left(\frac{R}{10km} \right)^{-1} \left(\frac{T}{10^{10}K} \right)^6 \left(\frac{\nu}{kHz} \right)^{-4} \left(\frac{B}{10^{15}G} \right)^{-2} \left(\frac{\sin^2 \chi}{g(\chi)} \right), \quad (20)$$

for $\omega\tau \ll 1$, and

$$T_{bulk} = 0.19s \left(\frac{M}{1.4M_\odot} \right)^{-1} \left(\frac{R}{10km} \right)^2 \left(\frac{T}{10^{10}K} \right)^{-6} \left(\frac{\nu}{kHz} \right)^{-2} \left(\frac{B}{10^{15}G} \right)^2 \left(\frac{\sin^2 \chi}{g(\chi)} \right), \quad (21)$$

for $\omega\tau \gg 1$, where

$$\omega\tau = 0.14 \times \cos \chi \left(\frac{\nu}{kHz} \right) \left(\frac{B}{10^{15}G} \right)^2 \left(\frac{R}{10km} \right)^2 \left(\frac{T}{10^{10}K} \right)^{-6} \left(\frac{M}{1.4M_\odot} \right)^{-4/3}. \quad (22)$$

and $g(\chi) \sim \sin^2 \chi$ for $\chi \ll 1$ and $g(\chi) \sim \cos^2 \chi$ for $\pi/2 - \chi \ll 1$. Note importantly that the timescale depends on the temperature.

In an early evolution of NS, the cooling due to Urca process (Owen et al. 1998; Page et al. 2006) is also important to include as the viscosity coefficients are temperature dependent and the star cools down from the initial temperature (at the end of the proto-NS phase) of around 10^{11} to 10^9 K in days. The modified-Urca cooling, given by Page et al. (2006) assuming the matter is too hot to become superconductor and/or superfluid, leads to the temperature profile as

$$T(t) = \left(\frac{6N_s}{C} t + \frac{1}{T_0^6} \right)^{-1/6}, \quad (23)$$

where T_0 is the temperature at time $t = 0$, and the constants $N_s = 10^{-32} \text{ s}^{-1} \text{ K}^{-8}$, $C = 10^{30} \text{ erg K}^{-2}$ and $T_0 = 10^{11} \text{ K}$. The characteristic timescale for cooling is given by Page et al. (2006) as,

$$T_{cooling} = 16 \left(\frac{C}{10^{30}} \right) \left(\frac{N_s}{10^{-32}} \right)^{-1} \left(\frac{T}{10^{10}} \right)^{-6} \text{ s}, \quad (24)$$

Therefore, the most general evolution equation for χ , including the effects of bulk viscosity, could be (Landau & Lifshitz 1987; Lindblom & Owen 2002; Lander & Jones 2017) given by

$$\begin{aligned}
 I_{z'z'} \frac{d\chi}{dt} &= -\frac{12G}{5c^5} (I_{zz} - I_{xx})^2 \Omega^4 \sin^3 \chi \cos \chi \\
 &- \frac{B_p^2 R_p^6 \Omega^2}{2c^3} \times \sin \chi \cos \chi F(x_0) + \zeta \epsilon_\Omega^2 \epsilon R^3 \frac{g(\chi)}{I_{zz} \sin \chi \cos \chi}, \\
 \epsilon_\Omega &= 0.21 \left(\frac{R}{10 \text{ km}} \right) \left(\frac{\nu}{\text{kHz}} \right)^2 \left(\frac{M}{1.4 M_\odot} \right)^{-1}, \\
 \zeta &= 4.2 \times 10^{33} \text{ g cm}^{-1} \text{ s}^{-1} \left(\frac{T}{10^{10} \text{ K}} \right)^{-6} \\
 &\left(\frac{M}{1.4 M_\odot} \right)^{10/3} \left(\frac{R}{10^6} \right)^{-10}, \quad (25)
 \end{aligned}$$

for $\omega\tau \ll 1$, and

$$\begin{aligned}
 \zeta &= 1.7 \times 10^{35} \text{ g cm}^{-1} \text{ s}^{-1} \left(\frac{T}{10^{10} \text{ K}} \right)^6 \left(\frac{M}{1.4 M_\odot} \right)^6 \\
 &\left(\frac{B}{10^{15} \text{ G}} \right)^{-4} \left(\frac{\nu}{\text{kHz}} \right)^{-2} \left(\frac{R}{10 \text{ km}} \right)^{-14} \left(\frac{1}{\cos^2 \chi} \right), \quad (26)
 \end{aligned}$$

for $\omega\tau \gg 1$. The above equation, along with the evolution of Ω (which remains unchanged as before), needs to be solved for the full time evolution of the obliquity angle.

Here bulk viscosity is assumed for a non-superfluid NS made only of neutrons, protons and electrons (Lander & Jones 2018). However, below certain temperature, the hyperons may appear in the core when it becomes superfluid, which significantly increases the bulk viscosity (Jones 1976; Lindblom & Owen 2002), hence the calculation is most conservative.

As ζ and the corresponding effect in the evolution of χ steeply depend on T , due to the cooling of proto-NS, effects of ζ suppress very fast. Therefore, practically NSs under consideration hardly become an orthogonal rotator and, hence, electromagnetic and GW radiations play the main role to evolve χ as discussed in the previous section.

However, if T would remain constant for a long time, the obliquity angle could increase and reach 90° . If the NS has a pure toroidal magnetic field, e.g., $B_{max}^{tor} \sim 9 \times 10^{16} \text{ G}$ (and much smaller poloidal magnetic field $B_{max}^{pol} \sim 5 \times 10^{14} \text{ G}$), it would tend to become an orthogonal rotator in a smaller timescale (e.g., in a few hours) due to viscous effect, when $T = 10^{10} \text{ K}$, compared to the time the effects due to electromagnetic and gravitational radiations would take to make it an aligned rotator (e.g., ~ 50 years). However, eventually, in a long run, χ would only decrease when electromagnetic and/or gravitational effects start playing a role, stopping any GW and electromagnetic radiation.

We also explore, for completeness, the χ evolution due to electromagnetic and/or gravitational radiations only with its initial value 30° . Fig 18 shows that the timescale changes between the initial $\chi = 3^\circ$ and 30° only by a few factors.

7 SENSITIVITY OF CONTINUOUS GRAVITATIONAL WAVE DETECTORS

We study the plausibility of instantaneous GW detection from isolated NSs by some existing and upcoming detectors.

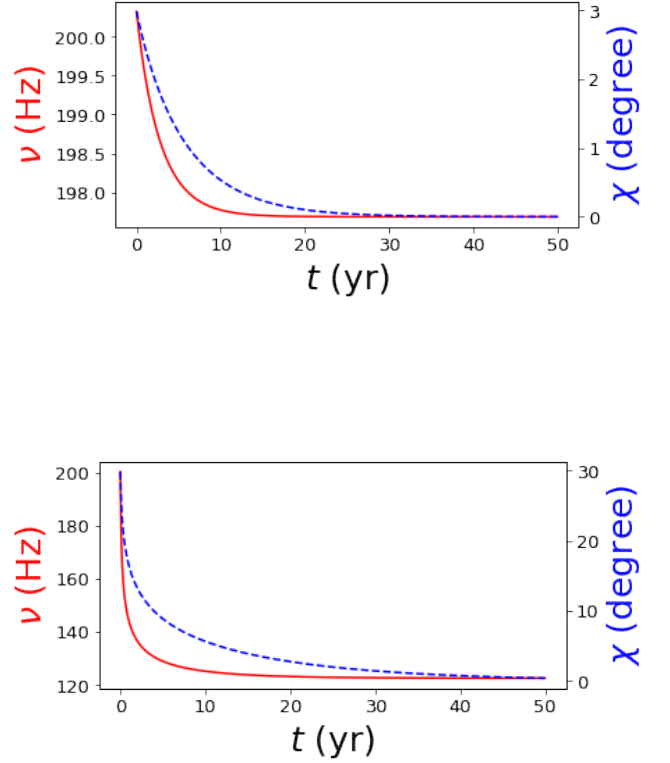


Figure 18. Variations of ν and χ with time for $B_{max}^{tor} \sim 9 \times 10^{16} \text{ G}$ (and $B_{max}^{pol} \sim 5 \times 10^{14} \text{ G}$), initial $\nu = 200 \text{ Hz}$, and $\chi = 3^\circ$ (upper panel) and $\chi = 30^\circ$ (lower panel). Red (solid) and blue (dashed) lines show the variations of ν and χ , respectively.

At present, extensive effort is going on to increase the sensitivity of detectors to detect CGWs emitted from various sources (Sieniawska & Bejger 2019). This can be done by calculating the SNR, thereby estimating the necessary observation time for the particular GW detector to detect these objects. A NS behaving like a pulsar can radiate CGWs at two frequencies. If the strength of the GW signal from the NS remains nearly unchanged during the observation time T , the cumulative SNR of the detector can be calculated coherently by discretizing the timescale finely, including information about phase for each grid (Jaranowski et al. 1998; Bennett et al. 2010), which takes very large computational time. However, in reality, the spin-down is so fast that ν and χ change rapidly; thus, GW strain also changes fast enough. In such a situation, the time integration is accomplished in time-stacks T_{stack} such that, in each stack, ν and χ remains nearly constant. The SNR is calculated coherently for each stack and then added incoherently to obtain the cumulative SNR. The total observation time T is divided into \mathcal{N} time-stacks such that $T = \mathcal{N}T_{stack}$. Also, in such a technique the phase information between the different stacks gets lost, thus it is called the incoherent search (see Maggiore 2007, for details of the technique). However, an incoherent search with a

time-stacking method is computationally efficient compared to the coherent search (Brady & Creighton 2000; Cutler et al. 2005) which is used for blind search of unknown pulsars (Leaci et al. 2012). Assuming ν , χ and h_0 remain nearly constant over each time-stack, adding \mathcal{N} such stacks, the cumulative SNRs is given by Maggiore (2007), as

$$\langle S/N \rangle = \sqrt{\langle S/N_\Omega^2 \rangle + \langle S/N_{2\Omega}^2 \rangle}, \quad (27)$$

where

$$\langle S/N_\Omega^2 \rangle = \frac{\sin^2 \zeta}{100} \frac{h_0^2 \sqrt{\mathcal{N}} T_{stack} \sin^2 2\chi}{S_n(\nu)} = \frac{\sin^2 \zeta}{100} \frac{h_0^2 T \sin^2 2\chi}{\sqrt{\mathcal{N}} S_n(\nu)} \quad (28)$$

and

$$\langle S/N_{2\Omega}^2 \rangle = \frac{4 \sin^2 \zeta}{25} \frac{h_0^2 \sqrt{\mathcal{N}} T_{stack} \sin^4 \chi}{S_n(2\nu)} = \frac{4 \sin^2 \zeta}{25} \frac{h_0^2 T \sin^4 \chi}{\sqrt{\mathcal{N}} S_n(2\nu)}, \quad (29)$$

where ζ is the angle between the interferometer arms and $S_n(\nu)$ is the detector's power spectral density (PSD) at the frequency ν with $\Omega = 2\pi\nu$. The data for PSD of various detectors are extracted from Moore et al. (2014) and Huang et al. (2020). For ground-based interferometers such as LIGO, VIRGO, KAGRA, Cosmic Explorer, etc. $\zeta = 90^\circ$ and for space-based interferometers such as Einstein Telescope $\zeta = 60^\circ$. Note that the average is over all possible angles, including i , which determines the object's orientation with respect to the celestial sphere reference frame.

Note that, in such a stacking technique, the SNR reduces by a factor $\mathcal{N}^{1/4}$ compared to the continuous integration in a full coherent search. Here we use the stacking method with $T_{stack} \approx 3$ hr. Also, in such a long time, the antenna pattern may change with time and there might be movement of antenna itself, which may lead to change in SNR, which will make the computation even more challenging (Maggiore 2007). Hence, while $\text{SNR} \sim 11$ is the appropriate threshold for the short-duration binary inspiral, due to the larger effective number of templates for the continuous search, it is computationally more challenging. This suggests to increase the threshold value of SNR (Dergachev & Papa 2021) to > 11.4 (Abbott et al. 2004; Maggiore et al. 2020; Cieřlar et al. 2021) for CGW; thus we set the threshold value for SNR to be 12 for more than 95% detection efficiency (Regimbau et al. 2012; Abbott et al. 2016b).

7.1 Possible detection of massive poloidally dominated neutron star pulsars

We solve equations (13) and (14) simultaneously to obtain $\Omega(t)$ and $\chi(t)$ assuming poloidal field dominated NSs and then calculate the cumulative SNR for various detectors (Kalita et al. 2020, 2021). Fig. 19 shows the SNR as a function of time for poloidal field dominated NSs with different field strengths at pole, i.e. 10^{15} G and 10^{12} G. B_P is larger in the first case; thus, Ω and χ decrease rapidly with time due to the large L_D . In the stacking method, the power of the GW signal for each stack is added up; thus, SNR increases for about one month and eventually saturates, as seen in Fig. 19. This happens because when Ω and χ decrease significantly, the strength of GW amplitude

also decreases; thus, the power for later stacks decreases. Hence, adding more stacks with comparatively less power does not efficiently change the cumulative SNR. However, when B_P is smaller, L_D is lower, and the SNR always increases with time for 1 yr because both Ω and χ remain nearly constant over the integration time, as seen in Fig. 19. It is however found that none of the detectors will be able to detect such NSs even after 1 yr of integration time. This is because the magnetic field $\approx 10^{14}$ is tiny for NS to produce sufficient deformation for GW radiation. The rotation rate $\nu = 100$ Hz is also quite small, which affects GW amplitude ($h_0 \propto \epsilon \Omega^2$). Now, if we increase B_P which is around 1.2×10^{17} G (Table 6), although h_0 increases enough to be detectable instantaneously by most of the detectors, Ω and χ decay in a couple of seconds. Hence, it should be very rare to detect such NSs, and there is no point in calculating cumulative SNR which will always be saturated. If we increase ν for $B_P = 1.2 \times 10^{14}$ G, although h_0 increases, which might help increase SNR, Ω and χ decay faster, hence SNR saturates faster; finally, SNR of any detector will not be able to increase up to 12.

7.2 Possible detection of massive toroidally dominated neutron star pulsars

Fig. 20 shows the SNR as a function of time for toroidal field-dominated NSs with different field strengths. As XNS cannot handle suitable toroidally dominated mixed field configuration with rotation, we assume toroidal dominated NSs with a poloidal surface field which is negligible with respect to the maximum toroidal field B_{max} . Such a poloidal field cannot change the shape and size of the NS as effectively as the toroidal field. Therefore, we run it for purely toroidal magnetic fields to obtain the shape and size of the NS. As L_D is small, Ω and χ hardly change within a 1 yr period. Fig. 20 shows the SNR for NSs with $B_{max} = 1.4 \times 10^{17}$ G and 9×10^{16} G. For the first case, Cosmic Explorer will be able to detect it in some months of integration. For the second case, none of the detectors will be able to detect such NSs even after one year of integration, because, When the field strength decreases, the SNR decreases, as shown in Fig. 20. If we increase the rotation rate, Ω and χ decay faster; thus, SNR saturates faster. For initial $\nu = 200$ Hz, the SNR increases over 1 yr because the Ω and χ decrease slowly than that of $\nu = 500$ Hz, which is shown in Fig. 21, and thus, the (relatively) slowly rotating NS might be detectable by Cosmic Explorer while the (relatively) fast rotating NS will not be detectable by any of the detectors.

8 MAGNETIC BRAKING: MASS LOSS OF DIFFERENTIALLY ROTATING NEUTRON STARS

Differentially rotating NSs can support significantly more mass than their uniformly rotating counterparts. The remnant of a binary NS merger or core collapse in a supernova may produce a hypermassive differentially rotating NS (Shibata & Uryū 2000; Zwerger & Mueller 1997; Rampp et al. 1998) where the remnant's core rotates considerably faster than its equator. However, magnetic braking forces the fluid

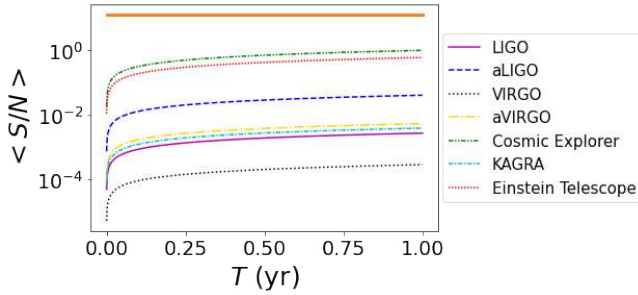
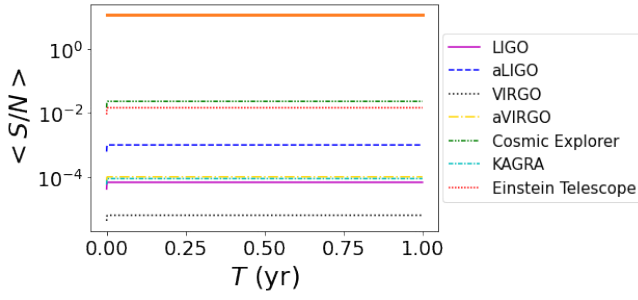


Figure 19. SNR for various detectors as a function of integration time for a poloidal magnetic field dominated NS with initial $\nu = 100$ Hz, $\chi = 3^\circ$, $B_P = 10^{15}$ G ($L_D > l_{GW}$; top panel) and $B_P = 10^{12}$ G ($L_{GW} > L_D$; bottom panel), for two cases from Table 6. The orange line corresponds to $\langle S/N \rangle = 12$.

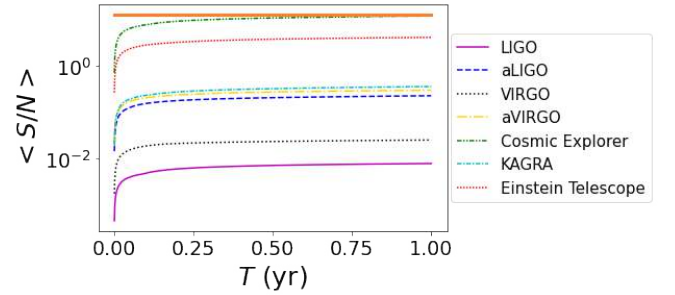
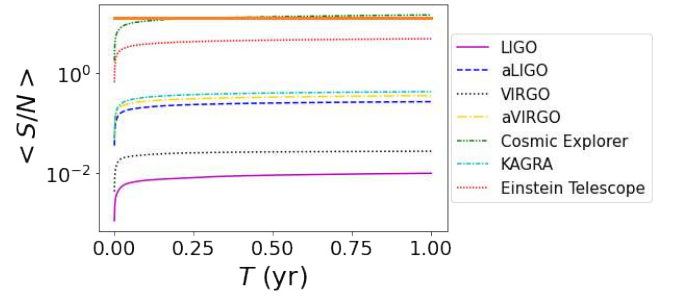


Figure 20. SNR for various detectors as a function of integration time for a toroidal magnetic field dominated NS with initial $\chi = 3^\circ$, initial $\nu = 500$ Hz, $B_{max} = 1.4 \times 10^{17}$ G (top panel) and $B_{max} = 9 \times 10^{16}$ G (bottom panel), for two cases from Table 7. The orange line corresponds to $\langle S/N \rangle = 12$.

to rotate as rigid body, while the vertical field is twisted, creating a powerful toroidal field. Then, the built-up magnetic stress back-reacts to drive differential rotation in the opposite direction, unwinding the magnetic field and then winding it up again in the opposite sense. This process will create Alfvén waves; the toroidal field component oscillates back and forth in a standing Alfvén wave pattern in the Alfvén timescale. The angular velocity profile oscillates around a state of uniform rotation, with uniform rotation taking place when the toroidal magnetic field is at maximum magnitude. At these times, a considerable amount of the rotational energy is converted to toroidal magnetic field energy.

In the presence of even small internal energy dissipation, e.g., by viscosity, the differentially rotating star will achieve a permanent state of uniform rotation by damping such dynamical oscillation. This is because the uniform rotation is the lowest energy state at a fixed angular momentum. The viscosity along with Alfvén waves carries away a significant amount of the angular momentum, and also some amount of magnetic energy will be converted into heat. This uniform rotation configuration cannot support the excess mass anymore and the star possibly will undergo some mass loss due to

core contraction and ejection of matter in the outer envelope to form a diffused ambient disk or trigger ejection of wind (Shapiro 2000; Cook et al. 2003; Liu & Shapiro 2003). This magnetic braking and angular momentum transport happen in a very first stage (a few tens of seconds) of proto-NSs, thus all radio pulsars are likely to be uniformly rotating.

The Alfvén timescale depends only on the strength of the seed field. Specifically, even with a weak initial poloidal field, along with viscosity, the azimuthal magnetic field will grow to a sufficiently high value, which is adequate to brake the differential motion and drive it to uniform rotation. The Alfvén timescale at each radial point of the star is given by

$$T_a(r) = \frac{r}{v_a(r)} = \frac{r\sqrt{4\pi\rho(r)}}{B(r)}, \quad (30)$$

where the density ρ and field B are functions of the radius, and thus Alfvén speed, v_a , is also a function of radius. We

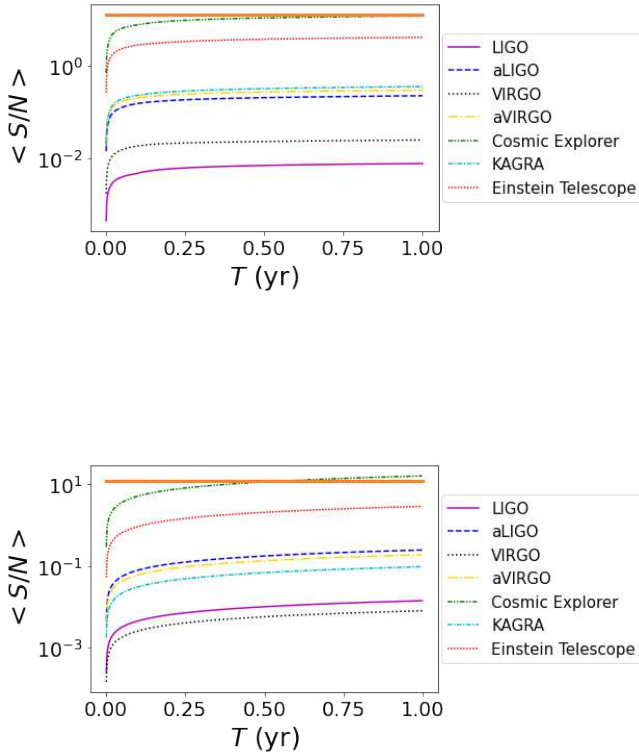


Figure 21. SNR for various detectors as a function of integration time for a toroidal magnetic field dominated NS with initial $\chi = 3^\circ$, $B_{\max} = 9 \times 10^{16}$ G, initial $\nu = 500$ Hz (top panel) and $\nu = 200$ Hz (bottom panel), for two cases from Table 7. The orange line corresponds to $\langle S/N \rangle = 12$.

have the profiles for ρ and B from *XNS* output. Thus we can integrate and obtain the value of T_a as

$$T_a = \int_0^R \frac{dr}{v_a} = \int_0^R \frac{dr \sqrt{4\pi\rho}}{B}. \quad (31)$$

The timescale for viscous dissipation after which the star becomes permanently uniformly rotating is given by [Cutler & Lindblom \(1987\)](#),

$$T_\nu \simeq 63.5 \left(\frac{R}{20 \text{ km}} \right)^{23/4} \left(\frac{T}{10^9 \text{ K}} \right)^2 \left(\frac{M}{3M_\odot} \right)^{-5/4} \text{ yr}. \quad (32)$$

The *XNS* code cannot handle differential rotation with a poloidal magnetic field. Thus, first we model a differentially rotating star without a magnetic field and calculate mass and radius. Then we model another two nonrotating stars with non-zero poloidal magnetic fields and zero fields, respectively, to show the effect of magnetic fields on mass and radius. From the result of [Liu & Shapiro \(2003\)](#), it is clear that the differentially rotating star will become uniform, and the star's final rotation will be the same as its progenitor's equatorial rotation rate. Thus we model another uniformly rotating star

with its progenitor's equatorial rotation rate and the poloidal magnetic field. Table 9 lists all the results. Table 9 indicates that the final star will be less massive after magnetic braking and viscous damping. Although we consider that the star has a purely poloidal field, in reality, it can have a toroidal magnetic field, which can be even stronger than the poloidal component. But Alfvén timescale only depends on the poloidal field, no matter how small it is, so we only consider the contribution due to the poloidal component. Shear viscosity also redistributes angular momentum. However, molecular viscosity in NS matter operates on a timescale of years, so it alone is much less effective in bringing the star into uniform rotation than with magnetic braking, unless the initial magnetic field is too weak. As the viscous damping happens in years of timescale, we consider the temperature to be $\simeq 10^9$ K, because the newborn hot NS with temperature $\simeq 10^{10}$ K would have been cooled down in days to months time.

We further consider polytropic EoS with polytropic index $\Gamma = 1.95$. As *XNS* does not have a provision yet to model differentially rotating poloidally magnetic NS, we first model NSs, as given in the first row of Table 9, with differential rotation keeping magnetic field zero, which can give us an idea about how mass changes with differential rotation. Then we build a model keeping rotation zero and with poloidal magnetic field, and the next one with no rotation, no magnetic field, given in the two successive rows in Table 9. The last two models will give us an idea about how mass changes due to magnetic field and, as we can clearly see, the chosen central field does not help to support (extra) mass at all. Therefore, we take the mass of the differentially rotating magnetized NS to be same as non-magnetized differentially rotating NS. The next model given in the fourth row of Table 9, which is magnetized uniformly rotating NS, shows us that it will be less massive after magnetic braking.

Note that in sections 4, 5, 6 and 8 we have shown how the NS and the GW signal from it evolve with time. However, it can be shown that the star remains dynamically stable during its evolution, e.g. from one *XNS* model to another, where the dynamical timescale is given by

$$T_d = \frac{1}{\sqrt{\rho}} \simeq \left(\frac{R^3}{M} \right) \simeq 0.15 \left(\frac{R}{20 \text{ km}} \right)^{3/2} \left(\frac{M}{3M_\odot} \right)^{-1/2} \text{ ms}. \quad (33)$$

Considering on average $M = 2M_\odot$, $R = 12$ km for the models we have used in this work, $T_d \simeq 8 \times 10^{-5}$ s, which is much much smaller than various evolution timescales involved here. Thus our assumption is correct.

9 CONCLUSIONS

After the detection of GW from the merger events, there is a great interest in the scientific community to discover CGW from isolated NSs and WDs. As NSs and WDs rotate at different ranges of frequencies, a different set of GW detectors (LIGO, VIRGO, aLIGO, aVIRGO, KAGRA Einstein Telescope, Cosmic Explorer for NSs and LISA, BBO, DECIGO, ALIA, TianQin for WDs) operating in their respective ranges of frequencies can detect them, and thus we can distinguish them as NSs or WDs. In the future, highly magnetized, rotating, massive NSs may be detected by Einstein Telescope,

Table 9. Differentially rotating and uniformly rotating poloidally dominated NSs, where ν_c and ν_{eq} are respectively central and equatorial frequencies.

$\rho_c(\text{g/cc})$	$M(M_\odot)$	$R_E(\text{km})$	$B_{max}(\text{G})$	$\nu_c(\text{Hz})$	$\nu_{eq}(\text{Hz})$	ME/GE	KE/GE	$T_a(\text{sec})$	$T_\nu(\text{year})$
10^{15}	2.08	11.6	0	3800	338	0	5.45×10^{-2}		
10^{15}	1.9	11.99	2×10^{16}	0	0	4.6×10^{-5}	0	0.035	3.5
10^{15}	1.9	11.99	0	0	0	0	0		
10^{15}	1.927	12.14	2×10^{16}	338	338	5×10^{-5}	9.37×10^{-3}		
10^{15}	2.08	11.6	0	3800	338	0	5.45×10^{-2}		
10^{15}	1.9	11.99	1.1×10^{13}	0	0	4.6×10^{-5}	0	70.7	3.5
10^{15}	1.9	11.99	0	0	0	0	0		
10^{15}	1.927	12.14	1.1×10^{13}	338	338	1.2×10^{-11}	9.37×10^{-3}		

which will confirm a direct detection of the NSs, and we can interpret their angular frequency, magnetic field, and internal constituents involved with EoS. However, none of them are detected so far by aLIGO, aVIRGO, which suggests us that those NSs are very challenging to detect. This is mainly because the GW amplitude decays significantly due to decay of Ω , χ and magnetic field; which can be seen from the results of Sections 4 and 5.

Also in Section 6, we have studied the possible effect of viscosity on the evolution of χ , which however strongly depends on temperature of the NS. We have found out that practically the NSs under consideration hardly become an orthogonal rotator due to viscosity. Hence, electromagnetic and GW radiations play the main role in evolution of χ .

We have used the Einstein equation solver *XNS* code to determine the structure of magnetized, rotating NSs. Subsequently we have studied the magnetic field decay throughout the star, assuming Ω and χ remain the same during the process, which is not though true in reality. However, the motivation in it is to see the change in GW strain solely due to magnetic field decay. Next, we have calculated the time scales related to pulsating NSs, i.e. the time-scale, after which the NS does not behave like a pulsar anymore due to dipole and GW radiation emitted by the NS. We have shown how GW strain decreases with time due to the Ω and χ decay, considering the magnetic field to remain constant during the process; which is a valid approximation, As we have seen from Sections 4 and 5, the time-scale at which magnetic field decays significantly is much longer than those of Ω and χ . In contrast, we can argue that long before magnetic field decay changes GW wave amplitude, the NS stops behaving as pulsar and thus will not be detectable anymore. Moreover, the proto NSs early after birth can be hypermassive due to differential rotation, which will become uniformly rotating less massive NS. Thus we are not expected to detect any hypermassive differentially rotating NS and, also, due to some mass loss, some NSs born as massive NS may not remain so for long. We have calculated all those time scales mentioned above for NSs in this paper, which were not explored simultaneously considering all the physics before this work to the best of our knowledge.

We have calculated the SNR for poloidally and toroidally dominated NSs, to detect the CGW for 1 yr of integration time. We know that to radiate electromagnetic dipole radiation, the NS, at least in its surface, should primarily contain

a poloidal magnetic field (Sousa et al. 2020). The results from Section 7 suggest that many of these massive NSs have high enough GW amplitude and, thus, they are well above the threshold SNR for some detectors. However, if the massive NSs are poloidally dominated and, thus, have high dipolar luminosities, χ decays very fast, so they cannot be detected for a longer duration by any of the detectors. However, if the NSs are toroidally dominated (so that $L_{GW} > L_D$) at the centre and has a minimal poloidal field at the pole, in reality, which should be the case (Wickramasinghe et al. 2014), they can be detected by the detectors for a long time. We have determined the detectors which would be able to detect these sources within 1 yr of observation with a large SNR. As we know that toroidal fields can change the size of NSs more than that the poloidal field does, the GW amplitude and thus SNR is higher for toroidally dominated massive NSs. Therefore, we can detect those NSs in a less detection timescale (or integration time), which is much more fruitful from an observational point of view because the possibility of detecting those NSs increases. This might be a fundamental breakthrough and can enhance our knowledge about their interior features and structures.

ACKNOWLEDGEMENTS

The authors thank Surajit Kalita of University of Cape Town for discussion about extracting ellipticity with *XNS* code and about time-stacking method to calculate cumulative SNR. They also thank Priti Gupta of Kyoto University (now in Indian Institute of Science) and Tejaswi Venumadhav Nerella of University of California Santa Barbara for discussion about SNR threshold value for CGW. Finally, thanks are due to the anonymous referee for the insightful comments and suggestions towards improving our manuscript.

DATA AVAILABILITY

The data underlying this article will be shared on reasonable request to the corresponding author.

REFERENCES

Abbott B., et al., 2004, *Phys. Rev. D*, **69**, 082004

- Abbott B. P., et al., 2016a, *Phys. Rev. Lett.*, **116**, 241103
- Abbott B. P., et al., 2016b, *Phys. Rev. Lett.*, **116**, 131103
- Abbott B. P., et al., 2017a, *Phys. Rev. Lett.*, **118**, 221101
- Abbott B. P., et al., 2017b, *Phys. Rev. Lett.*, **119**, 141101
- Abbott B. P., et al., 2017c, *Phys. Rev. Lett.*, **119**, 161101
- Abbott B. P., et al., 2017d, *Phys. Rev. Lett.*, **119**, 161101
- Abbott B. P., et al., 2017e, *ApJ*, **851**, L35
- Abbott B. P., et al., 2018, *Phys. Rev. Lett.*, **121**, 161101
- Abbott B. P., et al., 2019a, *Phys. Rev. X*, **9**, 011001
- Abbott B. P., et al., 2019b, *Phys. Rev. D*, **99**, 122002
- Abbott B. P., et al., 2019c, *Phys. Rev. D*, **100**, 024004
- Abbott B. P., et al., 2019d, *ApJ*, **882**, L24
- Abbott R., et al., 2020, *ApJ*, **896**, L44
- Akgün T., Reisenegger A., Mastrano A., Marchant P., 2013, *MNRAS*, **433**, 2445
- Antoniadis J., et al., 2013, *Science*, **340**, 448
- Balbus S. A., Hawley J. F., 1991, *ApJ*, **376**, 214
- Baym G., Pethick C., Pines D., 1969, *Nature*, **224**, 673
- Bennett M. F., van Eysden C. A., Melatos A., 2010, *MNRAS*, **409**, 1705
- Bhattacharya M., Hackett A. J., Gupta A., Tout C. A., Mukhopadhyay B., 2022, *ApJ*, **925**, 133
- Bonanno A., Rezzolla L., Urpin V., 2003, *A&A*, **410**, L33
- Bonazzola S., Gourgoulhon E., 1996, *A&A*, **312**, 675
- Brady P. R., Creighton T., 2000, *Phys. Rev. D*, **61**, 082001
- Braithwaite J., 2006, *A&A*, **453**, 687
- Braithwaite J., 2007, *A&A*, **469**, 275
- Braithwaite J., 2009, *MNRAS*, **397**, 763
- Brandenburg A., 2001, *ApJ*, **550**, 824
- Brandenburg A., Subramanian K., 2005, *Phys. Rep.*, **417**, 1
- Chatzioannou K., 2020, *General Relativity and Gravitation*, **52**, 109
- Chau W. Y., Henriksen R. N., 1970, *ApJ*, **161**, L137
- Chu P.-C., Chen L.-W., Wang X., 2014, *Phys. Rev. D*, **90**, 063013
- Cieřlar M., Bulik T., Curylo M., Sieniawska M., Singh N., Beijer M., 2021, *A&A*, **649**, A92
- Cioffi R., Rezzolla L., 2013, *MNRAS*, **435**, L43
- Colpi M., Geppert U., Page D., 1999, *ApJ*, **529**, L29
- Cook J., Shapiro S., Stephens B., 2003, *ApJ*, **599**
- Cromartie H. T., et al., 2020, *Nature Astronomy*, **4**, 72
- Cutler C., 2002, *Phys. Rev. D*, **66**, 084025
- Cutler C., Lindblom L., 1987, *ApJ*, **314**, 234
- Cutler C., Gholami I., Krishnan B., 2005, *Phys. Rev. D*, **72**, 042004
- Dall'Osso S., Shore S. N., Stella L., 2009, *MNRAS*, **398**, 1869
- Davis L., Goldstein M., 1970, *ApJ*, **159**, L81
- Deb D., Mukhopadhyay B., Weber F., 2021, *ApJ*, **922**, 149
- Demorest P. B., Pennucci T., Ransom S. M., Roberts M. S. E., Hessels J. W. T., 2010, *Nature*, **467**, 1081
- Dergachev V., Papa M. A., 2021, *Phys. Rev. D*, **103**, 063019
- Duncan R. C., 1998, *ApJ*, **498**, L45
- Duncan R. C., Thompson C., 1992, *ApJ*, **392**, L9
- Ferrari V., 2010, *Classical and Quantum Gravity*, **27**, 194006
- Ferrario L., Melatos A., Zrake J., 2015, *Space Sci. Rev.*, **191**, 77
- Franzon B., Schramm S., 2017, *MNRAS*, **467**, 4484
- Fricke K., 1969, *A&A*, **1**, 388
- Friebe J., Rezzolla L., 2012, *MNRAS*, **427**, 3406
- Frisch U., Pouquet A., Leorat J., Mazure A., 1975, *Journal of Fluid Mechanics*, **68**, 769
- Glampedakis K., Jones D. I., Samuelsson L., 2011, *MNRAS*, **413**, 2021
- Goldreich P., Reisenegger A., 1992, *ApJ*, **395**, 250
- Gualtieri L., Cioffi R., Ferrari V., 2011, *Classical and Quantum Gravity*, **28**, 114014
- Guilet J., Müller E., 2015, *MNRAS*, **450**, 2153
- Herbik M., Kokkotas K. D., 2017, *MNRAS*, **466**, 1330
- Heyl J. S., Kulkarni S. R., 1998, *ApJ*, **506**, L61
- Huang S.-J., et al., 2020, *Phys. Rev. D*, **102**, 063021
- Ioka K., Sasaki M., 2004, *ApJ*, **600**, 296
- Jaranowski P., Królak A., Schutz B. F., 1998, *Phys. Rev. D*, **58**, 063001
- Jones P. B., 1976, *Ap&SS*, **45**, 369
- Jones D. I., Andersson N., 2002, *MNRAS*, **331**, 203
- Kalita S., Mukhopadhyay B., 2019, *MNRAS*, **490**, 2692
- Kalita S., Mukhopadhyay B., Mondal T., Bulik T., 2020, *ApJ*, **896**, 69
- Kalita S., Mondal T., Tout C. A., Bulik T., Mukhopadhyay B., 2021, *MNRAS*, **508**, 842
- Kiuchi K., Yoshida S., 2008, *Phys. Rev. D*, **78**, 044045
- Komatsu H., Eriguchi Y., Hachisu I., 1989, *MNRAS*, **237**, 355
- Landau L., Lifshitz E., 1987, *Fluid Mechanics: Volume 6. No. v. 6*, Elsevier Science, <https://books.google.co.in/books?id=eVKbCgAAQBAJ>
- Lander S. K., 2013, *Phys. Rev. Lett.*, **110**, 071101
- Lander S. K., Jones D. I., 2012, *MNRAS*, **424**, 482
- Lander S. K., Jones D. I., 2017, *MNRAS*, **467**, 4343
- Lander S. K., Jones D. I., 2018, *MNRAS*, **481**, 4169
- Lander S. K., Jones D. I., 2020, *MNRAS*, **494**, 4838
- Lattimer J. M., 2012, *Annual Review of Nuclear and Particle Science*, **62**, 485
- Leaci P., (for the LIGO Scientific Collaboration the Virgo Collaboration) 2012, *Journal of Physics: Conference Series*, **354**, 012010
- Lindblom L., Owen B. J., 2002, *Phys. Rev. D*, **65**, 063006
- Liu Y. T., Shapiro S., 2003, *Phys. Rev. D*, **69**
- Lorimer D. R., 2008, *Living Reviews in Relativity*, **11**, 8
- Lü H.-J., Zou L., Lan L., Liang E.-W., 2018, *MNRAS*, **480**, 4402
- Maggiore M., 2007, *Gravitational Waves. Vol. 1: Theory and Experiments*. Oxford Master Series in Physics, Oxford University Press
- Maggiore M., et al., 2020, *J. Cosmology Astropart. Phys.*, **2020**, 050
- Markey P., Tayler R. J., 1974, *MNRAS*, **168**, 505
- Mastrano A., Suvorov A. G., Melatos A., 2015, *MNRAS*, **447**, 3475
- Melatos A., 2000, *MNRAS*, **313**, 217
- Michel F. C., Goldwire H. C. J., 1970, *Astrophys. Lett.*, **5**, 21
- Miller M. C., 2021, in Belloni T. M., Méndez M., Zhang C., eds, *Astrophysics and Space Science Library Vol. 461, Astrophysics and Space Science Library*. pp 1–51, doi:10.1007/978-3-662-62110-3_1
- Miralles J. A., Pons J. A., Urpin V. A., 2000, *ApJ*, **543**, 1001
- Miralles J. A., Pons J. A., Urpin V. A., 2002, *ApJ*, **574**, 356
- Moffatt H. K., 1978, *Magnetic field generation in electrically conducting fluids*
- Mondal T., 2021, *ApJ*, **913**, L12
- Moore C. J., Cole R. H., Berry C. P. L., 2014, *Classical and Quantum Gravity*, **32**, 015014
- Mösta P., Ott C. D., Radice D., Roberts L. F., Schnetter E., Haas R., 2015, *Nature*, **528**, 376
- Mukhopadhyay B., Bhattacharya M., 2022, *Particles*, **5**, 493
- Mukhopadhyay B., Rao A. R., Bhatia T. S., 2017, *MNRAS*, **472**, 3564
- Obergaulinger M., Cerdá-Durán P., Müller E., Aloy M. A., 2009, *A&A*, **498**, 241
- Owen B. J., Lindblom L., Cutler C., Schutz B. F., Vecchio A., Andersson N., 1998, *Phys. Rev. D*, **58**, 084020
- Page D., Geppert U., Weber F., 2006, *Nuclear Phys. A*, **777**, 497
- Piccinni O. J., et al., 2020, *Phys. Rev. D*, **101**, 082004
- Pili A. G., Bucciantini N., Del Zanna L., 2014, *MNRAS*, **439**, 3541
- Pons J. A., Miralles J. A., Geppert U., 2009, *A&A*, **496**, 207
- Rampp M., Mueller E., Ruffert M., 1998, *A&A*, **332**, 969
- Rather I. A., Rahaman U., Dexheimer V., Usmani A. A., Patra S. K., 2021, *ApJ*, **917**, 46
- Regimbau T., et al., 2012, *Phys. Rev. D*, **86**, 122001
- Rembiasz T., Guilet J., Obergaulinger M., Cerdá-Durán P., Aloy M. A., Müller E., 2016, *MNRAS*, **460**, 3316
- Riles K., 2017, *Modern Physics Letters A*, **32**, 1730035
- Shapiro S. L., 2000, *ApJ*, **544**, 397

- Shibata M., Uryū K. b. o., 2000, *Phys. Rev. D*, 61, 064001
- Shultz M., Rivinius T., Wade G. A., Alecian E., Petit V., the BinaMlCS Collaboration 2017, *MNRAS*, 475, 839
- Sieniawska M., Bejger M., 2019, *Universe*, 5, 217
- Sinha M., Sedrakian A., 2015, *Phys. Rev. C*, 91, 035805
- Sousa M. F., Coelho J. G., de Araujo J. C. N., 2020, *MNRAS*, 492, 5949
- Subramanian S., Mukhopadhyay B., 2015, *MNRAS*, 454, 752
- Suvorov A. G., Mastrano A., Geppert U., 2016, *MNRAS*, 459, 3407
- Tayler R. J., 1973, *MNRAS*, 161, 365
- Tayler R. J., 1980, *MNRAS*, 191, 151
- Thompson C., Duncan R. C., 1993, *ApJ*, 408, 194
- Thompson C., Murray N., 2001, *ApJ*, 560, 339
- Tilley D. R., Tilley J., Zimmermann W., 2019.
- Wickramasinghe D. T., Tout C. A., Ferrario L., 2014, *MNRAS*, 437, 675
- Woltjer L., 1964, *ApJ*, 140, 1309
- Wright G. A. E., 1973, *MNRAS*, 162, 339
- Yakovlev D. G., Urpin V. A., 1980, *Soviet Ast.*, 24, 303
- Zhang C. M., et al., 2011, *A&A*, 527, A83
- Zimmermann M., Szedenits E., 1979, *Phys. Rev. D*, 20, 351
- Zwerg T., Mueller E., 1997, *A&A*, 320, 209
- Şaşmaz Muş S., Çikintoğlu S., Aygün U., Andaç I. C., Ekşi K. Y., 2019, *ApJ*, 886, 5

This paper has been typeset from a \LaTeX file prepared by the author.